

Neptune's spatial brightness temperature variations from the vla and alma

Tollefson, Joshua; De Pater, Imke; Molter, Edward M.; Sault, Robert J.; Butler, Bryan J.; Luszcz-Cook, Stacia; DeBoer, David

DOI

[10.3847/PSJ/abf837](https://doi.org/10.3847/PSJ/abf837)

Publication date

2021

Document Version

Final published version

Published in

Planetary Science Journal

Citation (APA)

Tollefson, J., De Pater, I., Molter, E. M., Sault, R. J., Butler, B. J., Luszcz-Cook, S., & DeBoer, D. (2021). Neptune's spatial brightness temperature variations from the vla and alma. *Planetary Science Journal*, 2(3), Article 105. <https://doi.org/10.3847/PSJ/abf837>

Important note

To cite this publication, please use the final published version (if applicable). Please check the document version above.

Copyright

Other than for strictly personal use, it is not permitted to download, forward or distribute the text or part of it, without the consent of the author(s) and/or copyright holder(s), unless the work is under an open content license such as Creative Commons.

Takedown policy

Please contact us and provide details if you believe this document breaches copyrights. We will remove access to the work immediately and investigate your claim.



Neptune's Spatial Brightness Temperature Variations from the VLA and ALMA

Joshua Tollefson¹ , Imke de Pater^{1,2} , Edward M. Molter¹ , Robert J. Sault³ , Bryan J. Butler⁴ ,
Stacia Luszcz-Cook^{5,6} , and David DeBoer¹

¹ Department of Astronomy, University of California, Berkeley Berkeley, CA 94720, USA; jtollefs@berkeley.edu

² Faculty of Aerospace Engineering, Delft University of Technology, Delft 2629 HS, The Netherlands

³ School of Physics, University of Melbourne, Victoria, Australia

⁴ National Radio Astronomy Observatory, Socorro, NM, USA

⁵ Department of Astronomy, Columbia University, Pupin Hall, 538 West 120th Street, New York, NY 10027, USA

⁶ Astrophysics Department, American Museum of Natural History, Central Park West at 79th Street, New York, NY 10024, USA

Received 2020 April 1; revised 2021 April 9; accepted 2021 April 12; published 2021 June 8

Abstract

We present spatially resolved ($0''.1$ – $1''.0$) radio maps of Neptune taken from the Very Large Array and Atacama Large Millimeter/submillimeter Array between 2015 and 2017. Combined, these observations probe from just below the main methane cloud deck at ~ 1 bar down to the NH_4SH cloud at ~ 50 bar. Prominent latitudinal variations in the brightness temperature are seen across the disk. Depending on wavelength, the south polar region is 5–40 K brighter than the mid-latitudes and northern equatorial region. We use radiative transfer modeling coupled to Markov Chain Monte Carlo methods to retrieve H_2S , NH_3 , and CH_4 abundance profiles across the disk, though only strong constraints can be made for H_2S . Below all cloud formation, the data are well fit by $53.8^{+18.9}_{-13.4} \times$ and $3.9^{+2.1}_{-3.1} \times$ protosolar enrichment in the H_2S and NH_3 abundances, respectively, assuming a dry adiabat. Models in which the radio-cold mid-latitudes and northern equatorial region are supersaturated in H_2S are statistically favored over models following strict thermochemical equilibrium. H_2S is more abundant at the equatorial region than at the poles, indicative of strong, persistent global circulation. Our results imply that Neptune's sulfur-to-nitrogen ratio exceeds unity, as H_2S is more abundant than NH_3 in every retrieval. The absence of NH_3 above 50 bar can be explained either by partial dissolution of NH_3 in an ionic ocean at GPa pressures or by a planet formation scenario in which hydrated clathrates preferentially delivered sulfur rather than nitrogen onto planetesimals, or a combination of these hypotheses.

Unified Astronomy Thesaurus concepts: [Radio astrometry \(1337\)](#); [Neptune \(1096\)](#); [Planetary atmospheres \(1244\)](#); [Atmospheric composition \(2120\)](#)

1. Introduction

Neptune is the prototypical “ice giant”: a giant planet composed mainly of elements heavier than hydrogen and helium by mass, such as oxygen, nitrogen, carbon, and sulfur. Within the cold environment of Neptune, the products expected to form from these elements in the observable atmosphere include: H_2O , NH_3 , CH_4 , and H_2S . These molecules provide clues to the bulk composition of the planet, and so constraining their abundances is crucial for understanding Neptune's formation and thermal history.

Bright CH_4 clouds and aerosol hazes pervade Neptune's upper atmosphere. Optical and near-infrared wavelengths are sensitive to these components, limiting views in the atmosphere to pressures less than ~ 1 bar. H_2S and NH_3 condense at higher temperatures and pressures than CH_4 , meaning optical and near-infrared observations are blind to their deep abundances. Radio wavelengths probe beyond these shallow features, resolving the structure of Neptune's atmosphere down to ~ 50 bar. Thus, NH_3 and H_2S profiles can be constructed by inverting radio spectra. While early radio observations could only obtain disk-averaged measurements of Neptune, the observed high brightness temperatures longward of 10 cm required NH_3 , a prominent microwave absorber, to be

significantly depleted (de Pater & Massie 1985). This is possible if an NH_4SH cloud forms at ~ 50 bar and if the H_2S abundance exceeds that of NH_3 , resulting in the complete removal of NH_3 during the cloud's formation. In such an atmosphere, an H_2S abundance between 30 – $60 \times$ solar and an NH_3 abundance of $\sim 1 \times$ solar are required to fit the disk-averaged data (de Pater et al. 1991; DeBoer & Steffes 1996). Indeed, the detection of H_2S spectral features near $1.58 \mu\text{m}$ in the tropospheres of the ice giants implies that their deep bulk signal-to-noise ratio (S/N) is greater than one (Irwin et al. 2019b, 2019c).

de Pater et al. (2014) presented centimeter maps of Neptune from 2003, finding that the disk-averaged spectrum agreed with the abundances obtained from earlier radio observations. In addition, they found that the bright south polar cap must be significantly depleted in H_2S down to ~ 40 bar in order to match the observed brightness temperature at wavelengths of 0.7–6.0 cm. However, this study did not investigate brightness variations at other latitudes, as the sensitivity and resolution were not good enough to detect significant variations apart from those in the south polar cap.

In 2011, an upgrade of the Very Large Array (VLA) was completed. This expansion improved the continuum sensitivity by 5-to-20-fold and increased the wavelength coverage and bandwidth. This prompted a program to reobserve Neptune at centimeter wavelengths. The resulting maps, presented in this paper, show clear brightness temperature variations across the disk akin to that seen in millimeter maps produced from the



Original content from this work may be used under the terms of the [Creative Commons Attribution 4.0 licence](#). Any further distribution of this work must maintain attribution to the author(s) and the title of the work, journal citation and DOI.

Table 1
Summary of VLA Observations

| Wavelength (cm) | Frequency (GHz) | Band | Beam Size (arcsec ²) | Resolution (km ²) ^a | Time on Source (minutes) |
|-----------------|-----------------|-----------|----------------------------------|--|--------------------------|
| 0.9 | 32.958 | <i>Ka</i> | 0.12 × 0.12 | 2486 × 2486 | 156.0 |
| 2.0 | 14.880 | <i>Ku</i> | 0.25 × 0.25 | 5179 × 5179 | 136.8 |
| 3.0 | 9.869 | <i>X</i> | 0.35 × 0.26 | 7251 × 5387 | 139.8 |
| 5.1 | 5.861 | <i>C</i> | 0.56 × 0.45 | 11,603 × 9324 | 82.8 |
| 9.7 | 3.096 | <i>S</i> | 0.98 × 0.79 | 20,305 × 16,369 | 82.2 |

Note.

^a Resolution at sub-observer location, assuming equatorial and polar radii of 24,766 km and 24,323 km, respectively (Lindal 1992).

Atacama Large Millimeter/submillimeter Array (ALMA; Tollefson et al. 2019). The mm and cm wavelengths probe between ~ 1 bar and 50 bar on Neptune, meaning the most complete picture of Neptune’s upper atmosphere to date can be reconstructed by synthesizing these data. As NASA and ESA debate the merits of a next-decade ice giant mission, a firm handle on the uncertainties in the composition and dynamics of Neptune’s upper atmosphere are critical (Hofstadter et al. 2019). Just how well are the quantities of N, S, C, P, and O constrained from ground-based observations, in situ, and orbital measurements, and how does the amount and distribution of condensibles affect the observed atmospheric dynamics (Atreya et al. 2019; Hueso & Sánchez-Lavega 2019; Fletcher et al. 2020)? Do our uncertainties on these elements necessitate an instrument like Juno’s Microwave Radiometer (MWR; Janssen et al. 2017) on a future spacecraft to Neptune (Rymer et al. 2020)? What bands and configurations would be most useful for Neptune atmospheric science with the next generation VLA (ngVLA), and could it replace an MWR equivalent?

This paper is organized as follows. First, we present longitudinal-smear maps of Neptune taken with the expanded VLA in 2015 between 0.9 cm and 9.7 cm (Section 2). Next, we outline the structure of Neptune’s upper atmosphere and the free parameters used in our modeling (Section 3). We then combine these new VLA maps with 2003 VLA and ALMA observations of Neptune and use a Markov chain Monte Carlo (MCMC) implementation of the radiative transfer code Radio Berkeley Atmospheric Radiative transfer (Radio-BEAR) to obtain retrievals for the abundance profiles of Neptune’s condensibles (Section 4). Finally, we compare our findings to prior results (Section 5) and end with a summary of key takeaways (Section 6).

2. Observations

2.1. Data

This work makes use of two primary data sets: (1) ALMA millimeter observations of Neptune taken from 2016 to 2017, described in Section 2 of Tollefson et al. (2019); and (2) centimeter observations of Neptune taken with the upgraded VLA taken in 2015, described below.

We observed Neptune with the expanded VLA, an interferometer located near Socorro, New Mexico, on 2015 September 1 and 2. Maps were obtained at wavelengths of 0.9 cm (Band *Ka*), 2.0 cm (Band *Ku*), 3.0 cm (Band *X*), 5.1 cm (Band *C*), and 9.7 cm (Band *S*). The VLA consists of 27 antennas grouped into three arms of nine antennas to form a “Y”-shape. Every four months, the configuration is changed by moving the antennas along tracks. The “A” configuration is the VLA’s most

extended; the length of each arm is ~ 21 km, forming a maximum baseline of ~ 36 km. The maximum baseline is inversely related to the angular resolution, i.e., beam size, meaning variations across Neptune’s disk are most distinct in the A configuration. The observation set-up strongly impacts the shape of the beam. The symmetry of the VLA three-armed track, Neptune’s low declination at the time of the observation, and extended time on source causing the uv -plane sampling to fill out due to Earth’s rotation all contribute to the beams’ shapes.⁷ Neptune was observed on two days, each for 7 hr divided into many 5 minute scans that rotate through all wavelength bands. Thus, the degree of longitudinal smearing is high in the resulting maps as we observe Neptune throughout nearly an entire 16.11 hr rotation period (Warwick et al. 1989). Table 1 lists a summary of our observations.

We supplement these observations with VLA maps in 2003 from de Pater et al. (2014) in order to model Neptune’s disk-average temperature. These observations were taken in five bands for a total of 8 hr in each wavelength, including calibrators. Three of these bands (2 cm, *Ku*; 3.6 cm, *X*; 6 cm, *C*) were also taken in the “A” configuration, while the other two (0.7 cm, *Q*; 1.3 cm, *K*) were taken in the “BnA” configuration, which is a hybrid of the B and A configurations and was ideal for imaging Neptune at low declination.

2.2. Calibration and Imaging

The VLA observations were loaded from the NRAO data archive and converted for use in the MIRIAD software package (Sault et al. 1995). Flagging, calibration, and imaging were performed within MIRIAD. The calibrators used were 3C48 (flux density) and J2246–1206 (phase). In addition, self-calibration was performed to correct for short-term variability in the phases caused by fast atmospheric fluctuations. The self-calibration model used was a limb-darkened disk that best matched the observations. The limb-darkened profile is represented by the peak brightness temperature T_b multiplied by $\cos^k \theta$, where θ is the emission angle and k is a limb-darkening constant. Values for T_b and k were found at each wavelength such that the difference between the limb-darkened model disk and observations were minimized. Our final longitudinally smeared maps after subtracting the limb-darkened disk of Neptune are shown in Figure 1. While the images are “longitudinally smeared,” pixel-to-pixel variations are still present on the disk due to the presence of artifacts on

⁷ Further information on the various VLA configurations can be found in the VLA guides for proposers, Section 2: <https://science.nrao.edu/facilities/vla/docs/manuals/propvla/referencemanual-all-pages>. An introduction to radio astronomy fundamentals is available online via the Socorro Imaging Synthesis Workshop at <https://science.nrao.edu/science/meetings/2018/16th-synthesis-imaging-workshop/16th-synthesis-imaging-workshop-lectures>.

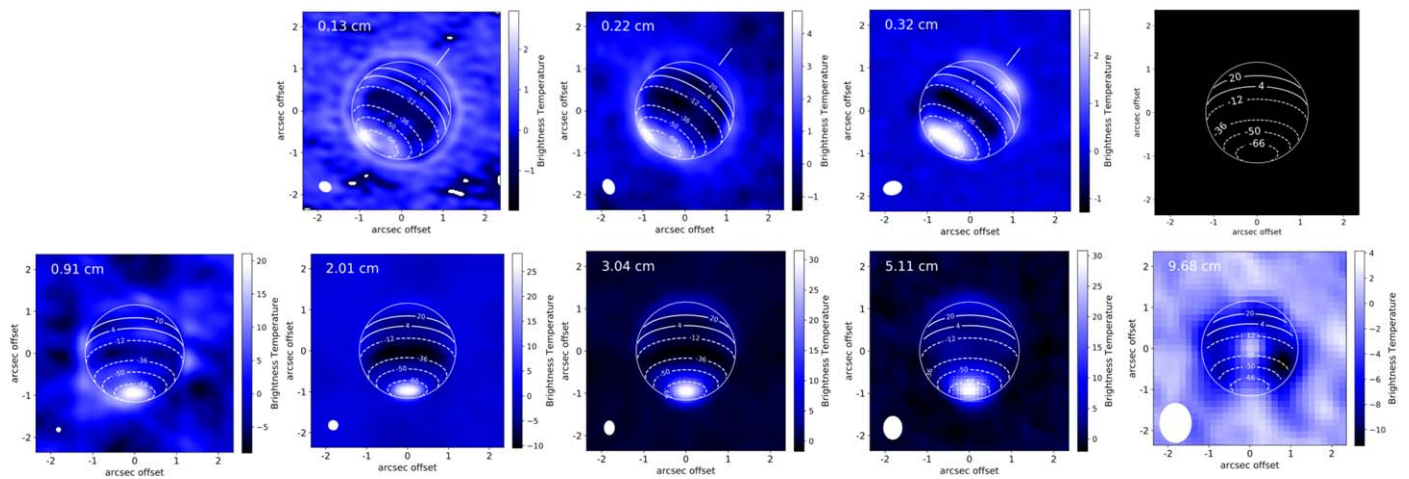


Figure 1. Longitude-smear maps of Neptune taken with ALMA (top row) and the upgraded VLA (bottom row). The color scale has been chosen to enhance the brightness contrasts across the disk. All maps are residuals, where a uniform limb-darkened model has been subtracted to highlight the temperature contrasts between latitudes. The north pole is indicated by a white line in the ALMA maps; the VLA maps are rotated so that the north pole is pointing upward. Contour lines delineate the latitude transitions between bands, with a grid over a blank disk shown in the upper right for clarity. Neptune’s disk is outlined with a white ellipse. The FWHM of the beam is indicated in white in the bottom left of each map.

the order of the beam size. Figure 2 plots the observed brightness temperature and residuals versus latitude along the central meridian of each disk. We divide Neptune into seven regions where the transitions in the brightness temperature variations are apparent: 90°S – 66°S , 66°S – 50°S , 50°S – 36°S , 36°S – 12°S , 12°S – 4°N , 4°N – 20°N , and 20°N – 50°N .

2.3. Error Estimation

The random noise in our VLA maps is calculated by averaging over four regions of the sky with boxes equal to the diameter of Neptune and taking the root-mean-square (rms). Values of rms range from 0.4 K to 2.0 K and are similar to the rms at a given latitude within the disk of a residual map. Table 2 lists our estimated errors in each band. The rms does not include systematic effects, such as errors in the bandpass or flux calibration. Uncertainties in the flux density are estimated at 5% or less in each band, so we use this as a conservative estimate for the absolute error in our disk-averaged temperature data.

3. Modeling

We generate models of Neptune’s brightness temperature using the radiative transfer (RT) code Radio-BEAR.⁸ Radio-BEAR generates synthetic spectra by solving the equation of radiative transfer through a model atmosphere. For a fuller description of Radio-BEAR, we refer the reader to de Pater et al. (2005, 2014, 2019), who outline how the model atmosphere is constructed from the bottom up and detail the absorption coefficients and line profiles for the species in this work. A description of the temperature profiles, cloud structure, and compositions considered in the model atmosphere is given below.

3.1. Temperature Profile

Temperature profiles are calculated from deep in the atmosphere upward, assuming either a dry or wet adiabat such that the profile matches the Voyager 2 temperature of 71.5 K at

1 bar (Lindal 1992). At pressures shallower than 1 bar, the temperature profile follows that derived from mid-infrared inversions by Fletcher et al. (2014). Temperatures, pressures, and altitudes are related through hydrostatic equilibrium. We assume that the atmosphere is in local thermodynamic equilibrium.

Figure 3 plots the wet and dry temperature profiles used in this paper. These are derived from a “nominal” atmosphere with $30\times$ protosolar abundances of H_2S , CH_4 , and H_2O , with $1\times$ NH_3 , no PH_3 , “intermediate” H_2 (see Section 3.5), and 100% relative humidity for each condensible species.⁹ Figure 3 also plots the nominal abundances of Neptune’s condensibles.

3.2. Cloud Structure

The condensibles in Neptune’s upper atmosphere are H_2S , CH_4 , H_2O , and NH_3 , all of which may condense to form clouds. Clouds expected to form on Neptune, from the bottom up, include: an aqueous ammonia solution (H_2O – NH_3 – H_2S), water-ice, ammonium hydrosulfide (NH_4SH), H_2S - or NH_3 -ice (whichever is left over after NH_4SH formation), and CH_4 -ice (Weidenschilling & Lewis 1973; Atreya & Wong 2005). The cloud density may affect microwave measurements. However, little is known about the cloud density on Neptune and clouds have been shown to not affect the microwave opacity on Jupiter (de Pater et al. 2019). Therefore, we ignore the effect of cloud opacity in our modeling and focus instead on the effect of gas opacity.

3.3. Condensible Species

The gas opacity of the microwave spectrum for gas giant atmospheres is dominated by H_2S , NH_3 , H_2O , and the collision-induced absorption (CIA) of H_2 (we include: H_2 – H_2 , H_2 – He , and H_2 – CH_4); (de Pater & Mitchell 1993). To form the NH_4SH cloud, H_2S and NH_3 are reduced in equal molar quantities until the product of their partial pressures reaches the equilibrium constant of the reaction forming NH_4SH . On Uranus and Neptune, the observation that NH_3

⁸ This code is available at: <https://github.com/david-deboer/radiobear>.

⁹ We use the protosolar values from Asplund et al. (2009): $\text{C}/\text{H}_2 = 5.90\text{E-}4$; $\text{N}/\text{H}_2 = 1.48\text{E-}4$; $\text{O}/\text{H}_2 = 1.07\text{E-}3$; $\text{S}/\text{H}_2 = 2.89\text{E-}5$.

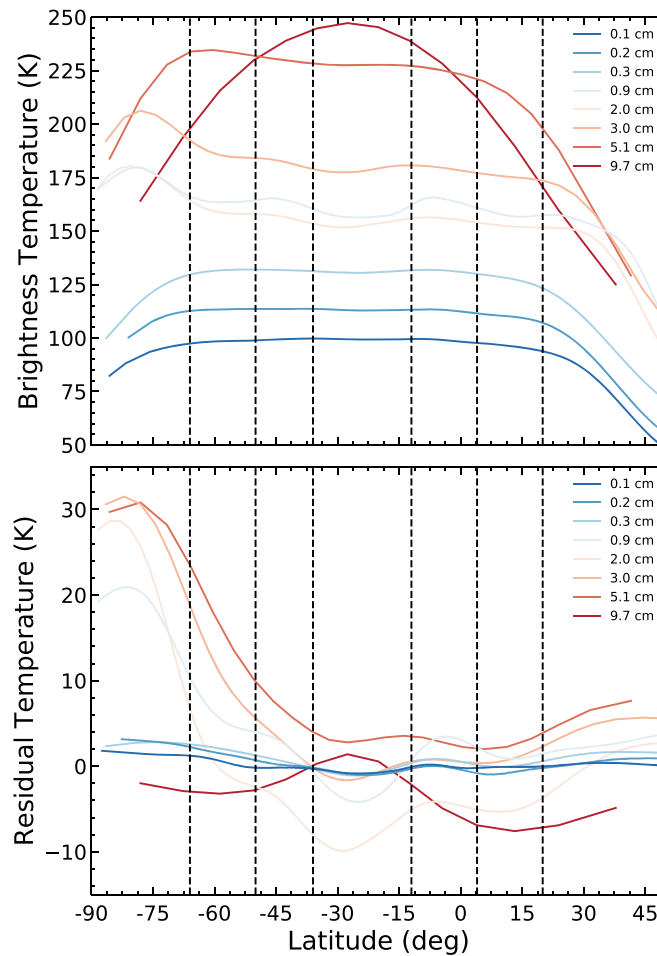


Figure 2. Neptune’s observed brightness temperature (top panel) and residual temperature (bottom panel) vs. latitude along the sub-observer longitude for each wavelength band (colored lines). The residual temperatures are taken from the residual maps shown in Figure 1 and are obtained by subtracting the observed brightness temperatures from best-fitting uniform limb-darkened disks, as described in Section 2.2 Dashed black lines delineate regions where brightness temperature variations are evident and define the latitude bins used in our modeling. Lines may not extend to 90°S due to limits in the resolution of the observation. The bump in the residual temperature at 9.7 cm is due to the poor resolution, as the large beam size impacts the limb-darkened fit.

is absent while H_2S is present above the NH_4SH layer (de Pater et al. 1991; Irwin et al. 2019b, 2019c; Molter et al. 2021) implies that this process takes up all of the NH_3 , leaving an excess of H_2S gas above the layer. Therefore, while NH_3 and H_2O are strong microwave absorbers, they are only abundant deeper than ~ 40 bar and only impact Neptune’s radio spectrum significantly at wavelengths longer than 10 cm. This is shown in Figure 3, which plots the normalized weighting functions at each observed wavelength assuming a nominal atmosphere. Our ALMA and VLA observations, with wavelengths shorter than 10 cm, are sensitive to pressures between 1 bar and 50 bar, peaking at altitudes at and above the aqueous NH_3 , H_2O -ice, and NH_4SH cloud formations. While NH_3 cannot be probed directly with our wavelength coverage, the chemical connection between H_2S and NH_3 means its abundance can be inferred. We therefore allow the NH_3 profile to vary, unlike in Tollefson et al. (2019). In our model, the formation of the NH_4SH cloud is governed by equilibrium chemistry described in Lewis (1969).

Our forward models allow the “deep” abundances of gaseous H_2S , NH_3 , and CH_4 to vary. We define “deep” as pressures below the NH_4SH cloud (forming at ~ 50 bar), but above aqueous solution cloud formation ($P > 100$ bar). For the nominal abundances, the solution cloud in full thermochemical

equilibrium removes about 5% of the interior H_2S and 25% of the interior NH_3 . From our retrieved values of “deep” H_2S and NH_3 , we obtain abundances below all cloud formation. We set no a priori restriction on the “deep” H_2S or NH_3 abundance, meaning either may survive above NH_4SH formation. H_2S or NH_3 , whichever persists, will then form an ice cloud and we allow its relative humidity to vary (see Figure 3, which shows H_2S -ice forming, as the “deep” H_2S abundance is larger than that of NH_3).

3.3.1. Phosphine (PH_3)

PH_3 is an important disequilibrium species on giant planets, tracing both chemistry and convective motion. In the deep atmosphere, PH_3 should oxidize to form P_4O_6 and dissolve in water (Fegley & Prinn 1986). In the upper atmosphere, PH_3 is photolyzed, and subsequent photochemical reactions may form to produce P_4 or complex polymers and compounds. Thus, PH_3 must be rapidly uplifted from the deep atmosphere to exist, making it useful as a passive tracer for both horizontal and vertical motions (Fegley & Prinn 1986; Fletcher et al. 2009).

PH_3 has not been detected on Uranus or Neptune, but if present is an important microwave absorber (DeBoer & Steffes 1996). The effect is most prominent at the PH_3 (1–0) rotation line at 266.9 GHz. The radio observations analyzed

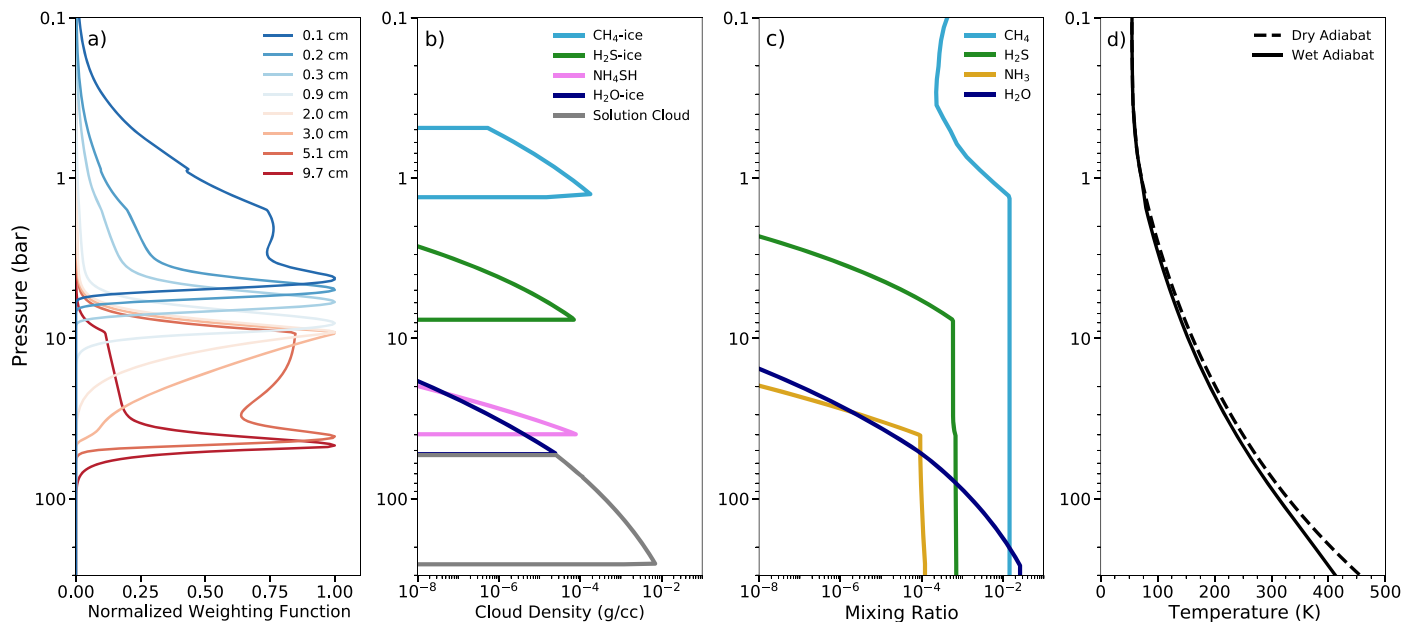


Figure 3. The normalized weighting functions at nadir for the wavelengths used in this study (a), showing the pressure at which each observation is sensitive. Different gas profiles, temperatures, and geometries will alter the peaks of the weighting functions. The clouds expected to form on Neptune as a function of their density and condensation pressures are shown in (b). The cloud density and condensation pressure are determined from thermochemical equilibrium and the nominal gas profiles, pictured in (c), which assume $30\times$ protosolar CH_4 (light blue), H_2S (green), and H_2O (dark blue), and $1\times$ protosolar NH_3 (yellow) at the deepest levels (below all cloud formation). The cloud and gas structure is also linked to the assumed temperature profile; both the dry and wet adiabatic temperature profiles for the nominal gas abundances are plotted in (d).

Table 2
Summary of Observed and Modeled Millimeter Disk-averaged Brightness Temperatures

| Center Frequency (GHz) | Facility | UT Date | Observed T_b^a (K) | Wet Disk Model T_b^b (K) | Noise ^c (K) |
|------------------------|----------|-------------|----------------------|----------------------------|------------------------|
| 3.096 | VLA | 2015 Sep 02 | 238.6 ± 11.5 | 223.8 | 1.3 |
| 4.915 | VLA | 2003 Jun 28 | 215.1 ± 10.8 | 206.7 | ... |
| 5.861 | VLA | 2015 Sep 01 | 214.3 ± 10.9 | 199.6 | 0.6 |
| 8.328 | VLA | 2003 Jun 27 | 183.3 ± 9.2 | 184.2 | ... |
| 9.869 | VLA | 2015 Sep 01 | 177.2 ± 8.9 | 177.7 | 0.4 |
| 14.880 | VLA | 2015 Sep 01 | 153.3 ± 7.7 | 161.4 | 0.7 |
| 14.990 | VLA | 2003 Jun 26 | 169.7 ± 8.5 | 161.1 | ... |
| 23.061 | VLA | 2003 Oct 11 | 150.6 ± 7.5 | 148.6 | ... |
| 32.958 | VLA | 2015 Sep 01 | 158.1 ± 7.9 | 141.7 | 2.0 |
| 42.827 | VLA | 2003 Oct 12 | 147.4 ± 7.4 | 138.0 | ... |
| 95.012 | ALMA | 2017 Jul 07 | 126.6 ± 6.3 | 121.6 | 0.1 |
| 96.970 | ALMA | 2017 Jul 07 | 126.0 ± 6.3 | 121.0 | 0.1 |
| 107.000 | ALMA | 2017 Jul 07 | 120.5 ± 6.0 | 117.9 | 0.2 |
| 109.000 | ALMA | 2017 Jul 07 | 118.8 ± 6.0 | 116.7 | 0.3 |
| 135.986 | ALMA | 2016 Oct 08 | 108.5 ± 5.4 | 105.8 | 0.3 |
| 137.924 | ALMA | 2016 Oct 08 | 108.0 ± 5.4 | 105.2 | 0.2 |
| 147.986 | ALMA | 2016 Oct 08 | 104.3 ± 5.2 | 102.7 | 0.2 |
| 149.986 | ALMA | 2016 Oct 08 | 104.5 ± 5.2 | 102.3 | 0.3 |
| 223.982 | ALMA | 2016 Oct 24 | 93.4 ± 4.7 | 92.1 | 0.4 |
| 225.982 | ALMA | 2016 Oct 24 | 93.0 ± 4.7 | 91.9 | 0.4 |
| 239.981 | ALMA | 2016 Oct 24 | 93.1 ± 4.7 | 90.0 | 0.6 |
| 241.981 | ALMA | 2016 Oct 24 | 92.8 ± 4.6 | 89.8 | 0.6 |

Notes.

^a The listed errors are the absolute errors, estimated at 5% from the calibrators.

^b The model brightness temperatures from the best-fitting wet adiabat MCMC retrievals.

^c Random errors defined as the rms on the sky. Values of rms errors are not available for the VLA 2003 data.

here only reach frequencies as high as 242 GHz (ALMA Band 6), meaning only the wings of the absorption line are detectable. However, if the abundance of PH_3 is large enough,

the pressure-broadened rotation line will be detectable in our highest frequency data. Thus, upper limits on the uplifted PH_3 abundance can be placed.

Our forward model assumes a constant PH_3 abundance until the temperature and pressure become so low that PH_3 condenses (~ 1 bar). We also only include PH_3 in our retrievals at latitudes where we expect upwelling and enriched condensibles, i.e., latitudes with comparatively cold brightness temperatures.

3.4. Ortho/para H_2

The ortho/para H_2 fraction also influences Neptune’s radio brightness temperature by modifying both the adiabatic lapse rate and the gas opacity (Trafton 1967; Wallace 1980; de Pater & Massie 1985; de Pater & Mitchell 1993). The ratio of ortho- to para-hydrogen in equilibrium depends on temperature; however, fast vertical mixing could bring the ratio of ortho and para states of hydrogen away from equilibrium and toward a “normal” ratio of three parts ortho to one part para. At latitudes where fast vertical mixing is unlikely, H_2 is presumed to exist in an “intermediate” state, proposed by Trafton (1967). In this case, the ortho and para states (which define the CIA properties) are set to the equilibrium value at the local temperature, while the specific heat is set near that of “normal” hydrogen. “Intermediate” hydrogen is discussed further in Massie & Hunten (1982), who provide physical reasons for the choice of this “intermediate” state. “Normal” hydrogen has been shown to decrease the microwave brightness temperature relative to “intermediate” hydrogen (de Pater & Mitchell 1993; Luszcz-Cook et al. 2013; Tollefson et al. 2019).

In our retrievals, we parameterize the state of H_2 as being between 0.0 and 1.0, where 0.0 represents the fully “normal” state and 1.0 is fully “intermediate.” Values in between represent a weighted average of the absorption coefficient between the two states. The specific heat is always set near to that of “normal” hydrogen, regardless of the parameter state.

3.5. Retrievals

In order to estimate uncertainties in our model parameters, we couple our Radio-BEAR models to MCMC simulations via a python implementation of the Goodman & Weare (2010) ensemble sampler called *emcee* (Foreman-Mackey et al. 2013). *emcee* has been used in near-infrared analyses of Uranus’ and Neptune’s hazes (de Kleer et al. 2015; Luszcz-Cook et al. 2016). We use similar log-likelihood Gaussian function and uniform/log-uniform priors as these authors; letting θ represent the free parameters in the model, the likelihood function $\ln p$ is:

$$\ln p(T_b|\nu, \theta, \sigma) = -0.5 \sum_{\nu_n} \left[\left(\frac{T_{b,n} - T_{b,m}}{\sigma_n} \right)^2 + \ln(2\pi\sigma_n^2) \right], \quad (1)$$

where $T_{b,n}$ is the observed brightness temperature, $T_{b,m}$ is the RT modeled brightness temperature, and σ_n is the total uncertainty, all at a given wavelength ν . This approach is in contrast to the methods in Tollefson et al. (2019), who compared the ALMA data to forward models of Neptune’s atmosphere. From these forward models, they obtained deep abundances of H_2S and CH_4 that fit the latitudinally varying brightness temperatures. A downside to this approach is that one can only rule out models that are improbable from χ^2 -statistics, meaning uncertainties are not retrieved.

We use 30 walkers and let MCMC run for between 4000 and 5000 steps. This run length ensured that the autocorrelation time was sufficiently shorter than the number of steps. All plots and tables show the distributions after burn-in, where the range of retrieved values approximately appear like their final probability density. The burn-in phase ends after 50% of the steps have been completed.

Observed and modeled brightness temperatures are obtained in each of the identified latitude bins listed in Section 2.2. One issue with RT models of particular regions on Neptune is that the finite size of the point-spread function (PSF) results in blurring of the disk. That is, the temperature within a particular latitude bin is a convolution of that latitude region, nearby latitudes, and sometimes the background sky. This effect is hard to model while conducting MCMC for two reasons: convolving the whole disk with the PSF is computationally expensive; and the model composition of the surrounding latitudes must be simultaneously known in order to obtain the exact temperature distribution across the disk. We circumvent this issue in two steps. First, we generate limb-darkened model disks of the best-fitting disk-averaged models (see Section 4.1) and then determine the brightness temperature in the region of interest with and without convolving the disk with the PSF. The ratio of the PSF convolved disk-averaged model temperature to that without convolution is called the PSF-scale. We multiply each MCMC retrieved model by the PSF-scale to obtain our final model brightness temperature incorporating the effect of convolution. This model temperature is fed into the *emcee* likelihood function. The effect of this scaling is smallest near the center of the disk and largest near the limb. Second, we add an error term to account for the uncertainty introduced by this approach,

$$\sigma_T^2 = \sigma_{\text{CAL}}^2 + \sigma_{\text{PSF}}^2, \quad (2)$$

where σ_T is the total error term used by *emcee* to calculate the likelihood function, σ_{CAL} is the 5% calibration error and σ_{PSF} is the error introduced by RT-modeling not accounting for the PSF. In our MCMC retrievals, we define an additional free parameter, σ , that is proportional to σ_{PSF} :

$$\sigma_{\text{PSF}} = \sigma \cdot T \cdot S, \quad (3)$$

where T is the observed brightness temperature and S is the product of the beam’s semimajor and semiminor axes. Adding an extra free parameter in the uncertainty is general practice in MCMC, as it encompasses unknown sources of error (for instance, via the introduction of PSF-scale). We find that the maximum retrieved values of σ_{PSF} are never larger than 5% of the product of T and S at disk center and 15% at the limb.

3.6. Atmospheric Models and Free Parameters

We consider four types of atmospheric models for these retrievals, depending on the latitude bin and expected dynamics, described below. Table 3 lists each of these models and the allowed free parameters. Figure 4 summarizes the effect of altering these parameters on the disk-averaged microwave spectrum of Neptune relative to the nominal model. Of note, the first two panels highlight the strong interaction between the deep H_2S and NH_3 abundances as a function of wavelength. NH_3 can exceed H_2S , resulting in NH_3 surviving NH_4SH cloud formation, by either sufficiently depleting H_2S

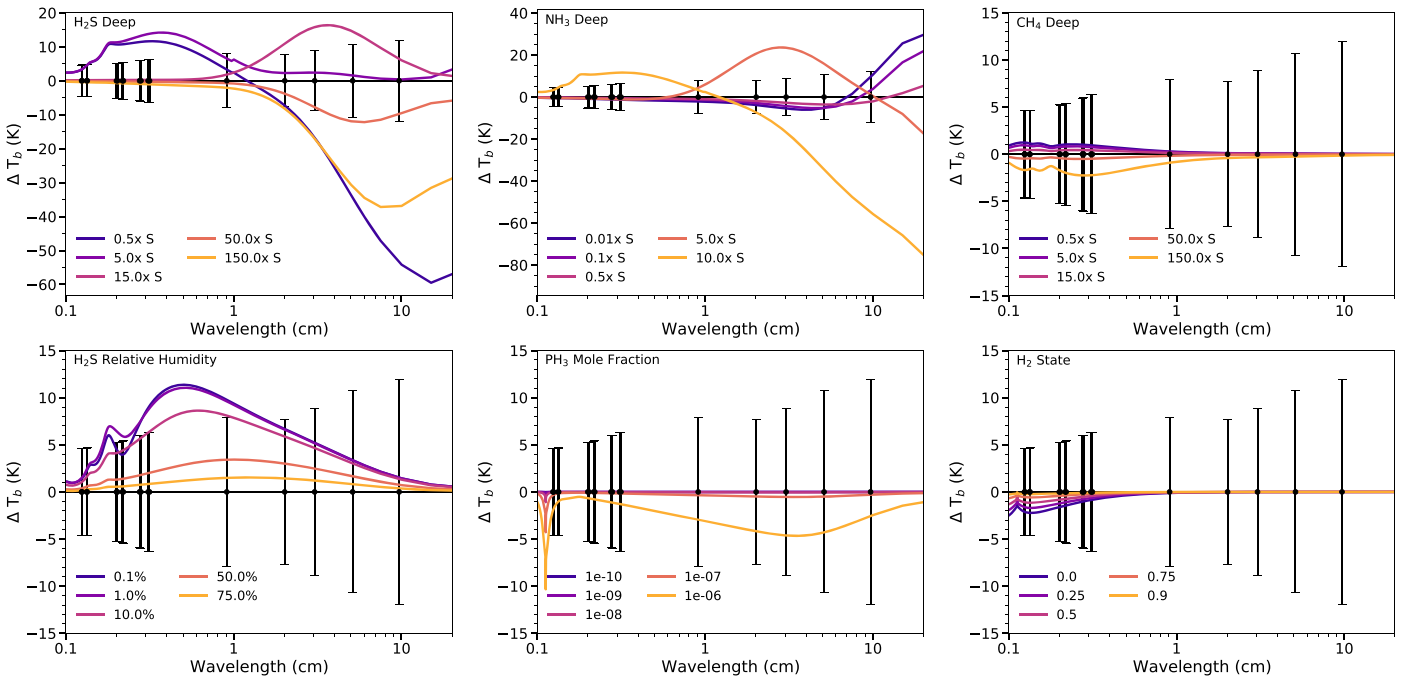


Figure 4. The effect of changing modeled parameters on Neptune’s disk-averaged microwave spectrum following a wet adiabat. Each panel shows how varying only the listed parameter from the nominal atmosphere alters the disk-averaged spectrum. ΔT_b is the difference from the nominal spectrum, with colored lines representing different values of the varied parameter. Positive ΔT_b values mean that the new model is warmer than the nominal model. The deep H_2S , NH_3 , and CH_4 abundances are given in terms of their protosolar enhancements (top row). The relative humidity of H_2S at its ice-cloud formation, the mole fraction of PH_3 , and the H_2 state (defined in Section 3.4) are, also (bottom row). Interesting behavior is seen in the deep H_2S panel, as both large and small amounts of H_2S ($0.5\times$ protosolar, blue vs. $150\times$ protosolar, yellow) produce negative ΔT_b longward of 1 cm, while only depleted amounts of H_2S result in positive ΔT_b in the millimeter, relative to the nominal model. These trends are explained in Section 3.6. The central wavelengths of our maps are plotted with black points. The error bars represent the calibration errors to give a sense of how important each parameter is in fitting the model to the data.

Table 3
Summary of Atmospheric Models and Free Parameters Used at Each Latitude Band

| Latitude Band | Model | H_2S Deep | NH_3 Deep | CH_4 Deep | PH_3 | H_2 State ^a | H_2S RH ^b | H_2S Frac ^c | NH_3 Frac ^c | CH_4 Frac ^c | P_{mix} | σ_{PSF} |
|---------------|--------------|---------------------------|--------------------|--------------------|---------------|---------------------------------|--------------------------------------|--|---------------------------------|---------------------------------|------------------|-----------------------|
| 4°N–20°N | Standard | × | × | × | 0.0 | Intermediate | × | N/A | N/A | N/A | N/A | × |
| 12°S–4°N | Standard | × | × | × | 0.0 | Intermediate | × | N/A | N/A | N/A | N/A | × |
| 36°S–12°S | Enriched | × | × | × | × | × | × | N/A | N/A | N/A | N/A | × |
| 50°S–36°S | Standard | × | × | × | 0.0 | Intermediate | × | N/A | N/A | N/A | N/A | × |
| 66°S–50°S | Standard | × | × | × | 0.0 | Intermediate | × | N/A | N/A | N/A | N/A | × |
| 90°S–66°S | Depleted | × | × | × | 0.0 | Intermediate | × | × | × | × | × | × |
| Global | Disk-average | × | × | × | 0.0 | Intermediate | × | N/A | N/A | N/A | N/A | Absent |

Notes. Parameters marked with an \times are varied in MCMC. If they are not varied, their set value is given instead, if applicable. In our retrievals, all free parameters are varied in \log_{10} -space apart from the H_2 state.

^a All retrieved parameters in this paper except H_2 State are varied in \log_{10} space.

^b RH stands for relative humidity. Supersaturated H_2S is allowed in Section 4.3.

^c Frac is the fractional abundance relative to the “deep” amount of the condensibles existing above the mixing pressure P_{mix} in the “Depleted” south polar model.

(blue line, $0.5\times S$, in the H_2S deep panel) or enriching NH_3 (yellow line, $10\times S$, in the NH_3 deep panel). The millimeter spectrum becomes brighter, as more NH_3 will react with more H_2S at NH_4SH formation, thereby reducing the total amount of H_2S above it. On the other hand, the centimeter spectrum becomes colder, as NH_3 gas is a stronger microwave absorber than H_2S gas. All other parameters have the strongest impact at $\lambda \leq 1$ cm. Note, however, that our ability to retrieve the deep CH_4 abundance is limited compared to that of H_2S . This is due to a combination of having less overall impact on the microwave opacity, lower than our calibration errors, and other sources like the H_2S relative humidity, PH_3 , and the H_2

state having comparable or stronger effects in millimeter wavelengths. The considered models are:

1. Enriched Atmosphere: Used for latitude bands that have relatively cold brightness temperatures, where enriched and upwelling air is expected. The “deep”¹⁰ abundances of H_2S , NH_3 , and CH_4 are allowed to vary. The NH_4SH , H_2S -ice, and CH_4 -ice clouds are allowed to form and the relative humidity of H_2S is varied. The PH_3

¹⁰ Again, “deep” is defined as pressures above the H_2O and aqueous solution clouds and below the NH_4SH cloud.

abundance is allowed to vary; a uniform vertical profile is assumed up to the saturation pressure of PH_3 . The ortho- to para- H_2 fraction is allowed to vary between 0.0 and 1.0, representing the range of fully “normal” to fully “intermediate” states. Both dry and wet adiabats are considered.

2. Depleted Atmosphere: Used for latitude bands that have relatively warm brightness temperatures, where depleted and downwelling air is expected. The “deep” abundance of condensibles is set to that of the enriched atmosphere at altitudes below the “mixing pressure,” P_{mix} . At shallower altitudes, the abundance of condensibles is varied by some fraction of the deep abundance. The final profiles for the condensibles look like step functions, with the transition at P_{mix} . We allow the formation of H_2S - and NH_3 -ice. Both dry and wet adiabats are considered.
3. Disk Average: The disk-averaged model for the atmosphere looks like that of the enriched, but we only let the “deep” abundances of H_2S , NH_3 , and CH_4 , and the relative humidity of H_2S , to vary. This model is done to compare to prior work and so both PH_3 and the H_2 state are not varied. We caution that disk-averaged retrievals poorly describe the physics within the planet. Both dry and wet adiabats are considered.
4. Standard: At other latitudes not fitting the above prescriptions, we model the atmosphere similar to the enriched atmosphere, as it follows standard cloud formation and thermochemical equilibrium unlike the depleted/downwelling atmosphere. Unlike the “Enriched” model, the PH_3 abundance and ortho/para H_2 state are not allowed to vary. Both dry and wet adiabats are considered.

4. Results

4.1. Disk-averaged Profiles

We calculate Neptune’s disk-average brightness temperature by totaling the flux density contained within Neptune’s disk plus the area extending out three times the model beam diameter past the limb. The apparent brightness temperature measured in interferometric imaging is less than the true value by an amount related to the cosmic microwave background (CMB). The CMB correction is applied following the procedure laid out in Appendix A of de Pater et al. (2014). These results are combined with measurements of Neptune’s disk-average brightness temperature from VLA 2003 (de Pater et al. 2014) and ALMA (Tollefson et al. 2019) to form our set of data used in MCMC retrievals. A summary of this data set is given in Table 2.

Figure 5 plots the best-fitting H_2S and NH_3 profiles and 500 random retrieved profiles from the posterior distribution for a wet adiabat. Figure 5 also shows the observed disk-averaged brightness temperatures versus wavelength, likewise plotting the best-fitting and 100 random retrieved model spectra assuming a wet adiabat. Table 4 lists the retrieved parameters. H_2S is more abundant than NH_3 in both the dry and wet thermal profiles. There is also significant positive correlation between the deep NH_3 and H_2S abundances. This is expected based on the NH_4SH cloud chemistry; retrievals with larger NH_3 require additional H_2S to remove the NH_3 during the NH_4SH reaction to match the observations probing above the NH_4SH cloud. The dry adiabat permits marginally larger

abundances of all condensibles throughout the upper atmosphere due to the need to increase the opacity in order to offset the higher temperatures.

4.2. 36°S – 12°S and 90°S – 66°S Profiles

The latitude band between 36°S and 12°S is dark in both the VLA maps presented here (Figure 1) and the ALMA residual maps. Low brightness temperatures imply increased opacity from Neptune’s condensibles. Conversely, Neptune’s south polar cap, between 90°S and 66°S , is warm in both data sets, implying a lower abundance of condensibles. Due to the lower abundance of condensibles, the peaks of the normalized weighting functions are deeper in the atmosphere than for the nominal model (Figure 3), meaning we are more sensitive to abundances of Neptune’s condensibles below the NH_4SH cloud at the south pole. As a result, we first obtain retrievals for the mixing pressure P_{mix} and abundances of condensibles over the south polar cap. The retrieved probability density functions for the condensible abundances below P_{mix} are then used as priors for the condensible abundance below the NH_4SH cloud in the cold mid-latitude band between 36°S and 12°S . The atmospheric models and free parameters used for these bands are described in Table 3 and Section 3.6.

The brightness temperatures fed into MCMC are obtained by averaging over all pixels that are within $\pm 60^\circ$ of the sub-observer longitude at each latitude band. Likewise, the modeled spectra are obtained using the average emission angle within this zonal average. The uncertainty is dominated by the flux calibration error. The term σ_{PSF} is also added to this uncertainty, though its effect is small compared to the calibration error.

Data for Neptune’s latitudinal variations are not available in the VLA 2003 maps apart from those at the south polar cap. We do not use these data, as the temperatures reported in de Pater et al. (2014) are the maximum temperatures within the south polar cap at each wavelength instead of the average.

Tables 5 and 6 list the 16th/50th/84th percentiles on the gas profile parameters for the simultaneous 36°S – 12°S and 90°S – 66°S models. If a parameter is not well constrained, the 97.5th percentile (2σ) upper limit is given instead. Corner plots showing the covariance and probability distribution for the free parameters are given in Figure 6, assuming the temperature profile at the south polar cap follows a wet adiabat. As in the disk-average results, there is significant correlation between the deep H_2S and NH_3 abundances. The presence of additional NH_3 at deep levels will lead to additional H_2S at the NH_4SH layer. However, H_2S is the primary absorber above the NH_4SH layer and so our data are very sensitive to its abundance. Therefore, an increased NH_3 abundance requires a compensating increase in the H_2S abundance. In addition, our results show that the H_2S profile is constrained at the cold mid-latitudes but unconstrained at the south pole. The NH_3 abundance below the NH_4SH cloud is somewhat constrained at each latitude band, though a long tail forms at low abundances for retrievals with less H_2S . In addition, P_{mix} is well constrained at the south polar cap and is in line with the NH_4SH condensation pressure. The retrievals also indicate a constant amount of NH_3 above P_{mix} at the south polar cap, though the median values are larger than the 12 ppb abundance required by de Pater et al. (2014) to best match their own observations.

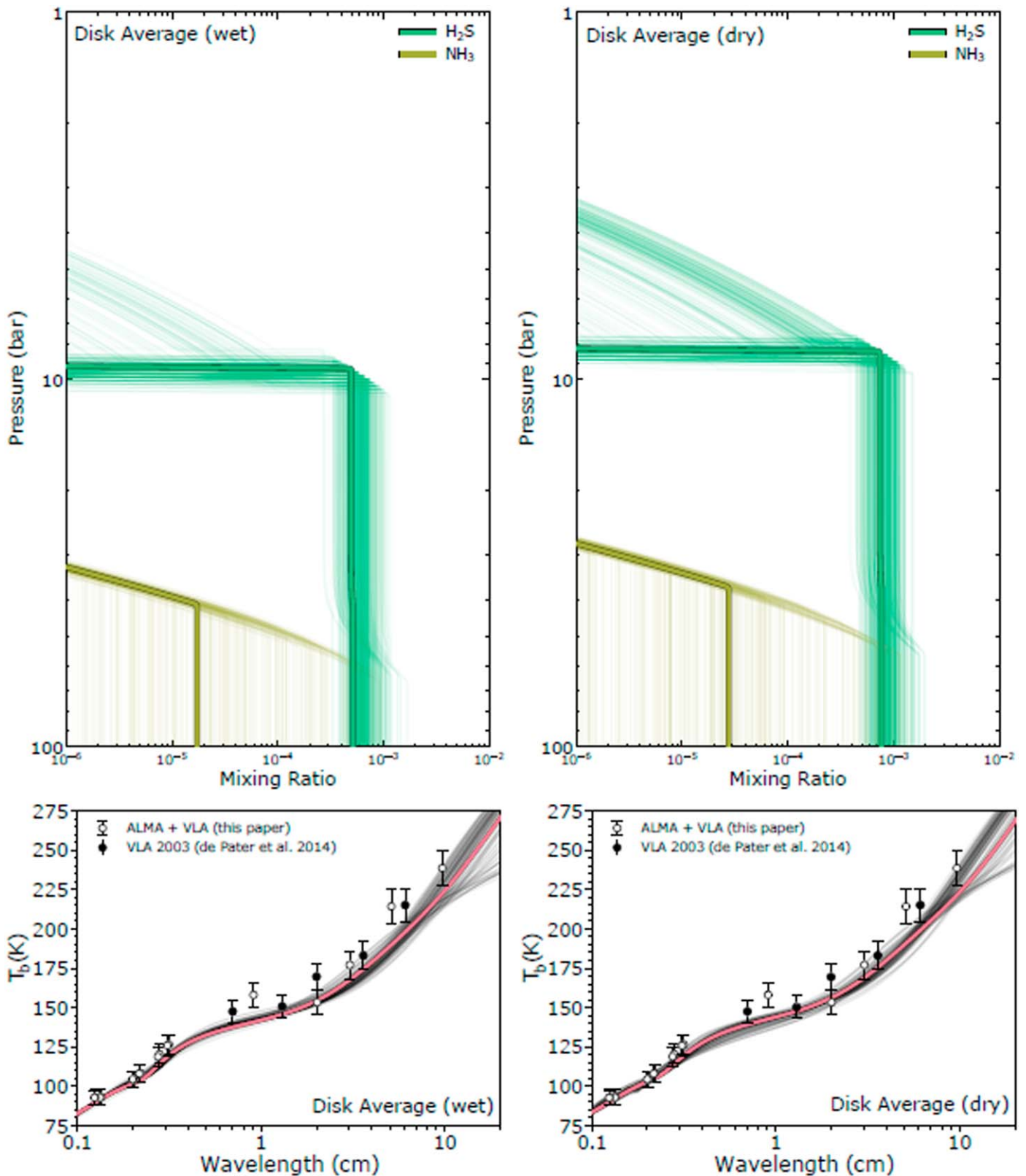


Figure 5. Top row: best-fitting H₂S (thick green) and NH₃ (thick yellow) profiles for the disk-average wet (left) and dry (right) adiabat models. Thin lines are 500 random retrieved profiles. Bottom row: disk-average data from VLA 2003 (de Pater et al. 2014; black circles) and from ALMA and the upgraded VLA (this paper, white circles). The thick red line is the best-fitting spectrum following a wet (left) and dry (right) adiabat. Thin black lines are also plotted, representing 100 random draws from the posterior.

The deep CH₄ abundance is only weakly constrained as its effect on the radio opacity is small compared to the calibration uncertainty (see Figure 4). Moreover, it competes with effects

from PH₃, the H₂ state, and the relative humidity of H₂S. At 36°S–12°S, we obtain an upper limit of 85.4× protosolar or 4.1% mixing ratio at the 2 σ level, assuming a wet adiabat

Table 4
MCMC Fit Results for the Disk-average Models

| Disk Average, Wet Adiabatic | | |
|---|------------------------------------|---|
| Parameter | Retrieved values | Protosolar Enhancement (\times Solar) |
| H ₂ S below NH ₄ SH | $6.3^{+1.9}_{-1.2} \times 10^{-4}$ | $26.8^{+8.1}_{-5.1}$ |
| NH ₃ below NH ₄ SH | $\leq 6.5 \times 10^{-4}$ | ≤ 5.4 |
| CH ₄ | $\leq 1.6 \times 10^{-2}$ | ≤ 33.3 |
| H ₂ S H_{rel} | $\leq 18\%$ | ... |
| H ₂ S below all clouds | $6.6^{+2.0}_{-1.3} \times 10^{-4}$ | $28.2^{+8.5}_{-5.4}$ |
| Disk Average, Dry Adiabatic | | |
| Parameter | Retrieved values | Protosolar Enhancement (\times Solar) |
| H ₂ S below NH ₄ SH | $8.8^{+2.0}_{-2.1} \times 10^{-4}$ | $37.5^{+9.4}_{-8.9}$ |
| NH ₃ below NH ₄ SH | Unconstrained | Unconstrained |
| CH ₄ | $\leq 1.3 \times 10^{-2}$ | ≤ 27.1 |
| H ₂ S H_{rel} | $\leq 75\%$ | ... |
| H ₂ S below all clouds | $9.3^{+2.1}_{-2.2} \times 10^{-4}$ | $39.4^{+9.9}_{-9.4}$ |

Note. The listed H₂S abundances below NH₄SH cloud formation are the 50th percentile of the posterior distributions with the error bars corresponding to the 16th and 84th percentiles, i.e., the 1σ uncertainties. NH₃, CH₄, and the relative humidity of H₂S are not well constrained in either model, and so the 97.5th percentile value, representing the 2σ upper limit, is given instead. Abundances below all cloud formation are estimated according to the discussion in Section 3.3.

Table 5
MCMC Results for the Simultaneous Fit to the 36°S–12°S and 90°S–66°S Bands Assuming a Wet Adiabatic

| 90°S–66°S, Wet Adiabatic | | |
|---|-------------------------------------|---|
| Parameter | Retrieved values | Protosolar Enhancement (\times Solar) |
| H ₂ S below P_{mix} | $0.3^{+15.7}_{-0.3} \times 10^{-4}$ | $1.3^{+65.6}_{-1.3}$ |
| NH ₃ below P_{mix} | $2.5^{+2.1}_{-2.1} \times 10^{-4}$ | $2.1^{+1.7}_{-1.8}$ |
| H ₂ S above P_{mix} | $2.7^{+9.3}_{-2.7} \times 10^{-7}$ | $1.2^{+3.9}_{-1.2} \times 10^{-2}$ |
| NH ₃ above P_{mix} | $3.3^{+2.8}_{-2.2} \times 10^{-7}$ | $2.8^{+2.3}_{-1.9} \times 10^{-3}$ |
| P_{mix} | 41^{+9}_{-7} bar | ... |
| 36°S–12°S, Wet Adiabatic | | |
| Parameter | Retrieved values | Protosolar Enhancement (\times Solar) |
| H ₂ S below NH ₄ SH | $8.3^{+2.5}_{-2.3} \times 10^{-4}$ | $35.4^{+14.9}_{-9.8}$ |
| NH ₃ below NH ₄ SH | $1.9^{+2.0}_{-1.7} \times 10^{-4}$ | $1.6^{+1.7}_{-1.4}$ |
| CH ₄ | $\leq 4.1 \times 10^{-2}$ | ≤ 85.4 |
| H ₂ S H_{rel} | $\leq 57\%$ | ... |
| PH ₃ | $\leq 8.2 \times 10^{-7}$ | ≤ 0.2 |
| H ₂ State | Unconstrained | ... |
| H ₂ S below all clouds | $8.7^{+2.6}_{-1.7} \times 10^{-4}$ | $37.3^{+15.7}_{-10.3}$ |
| NH ₃ below all clouds | $2.5^{+2.7}_{-2.3} \times 10^{-4}$ | $2.1^{+2.3}_{-1.9}$ |

Note. The deep abundances of H₂S, NH₃, and CH₄, and σ_{PSF} are the same in each region. Otherwise, parameters are varied according to Table 3. The listed values are the 50th percentile of the posterior distributions with the error bars corresponding to the 16th and 84th percentiles, i.e., the 1σ uncertainties. Parameters that are poorly constrained have their 97.5th percentile value listed instead, representing the 2σ upper limit. Abundances below all cloud formation are estimated according to the discussion in Section 3.3.

Table 6
As in Table 5, But Assuming a Dry Adiabatic in Each Region

| 90°S–66°S, Dry Adiabatic | | |
|---|-------------------------------------|---|
| Parameter | Retrieved values | Protosolar Enhancement (\times Solar) |
| H ₂ S below P_{mix} | $3.6^{+25.4}_{-3.3} \times 10^{-4}$ | $15.3^{+108.3}_{-8.9}$ |
| NH ₃ below P_{mix} | $3.8^{+2.2}_{-2.4} \times 10^{-4}$ | $3.2^{+1.8}_{-2.1}$ |
| H ₂ S above P_{mix} | $7.1^{+5.9}_{-2.8} \times 10^{-6}$ | $3.0^{+2.5}_{-1.0} \times 10^{-1}$ |
| NH ₃ above P_{mix} | $1.6^{+3.1}_{-1.3} \times 10^{-7}$ | $1.3^{+2.6}_{-1.0} \times 10^{-3}$ |
| P_{mix} | 33^{+6}_{-4} bar | ... |
| 36°S–12°S, Dry Adiabatic | | |
| Parameter | Retrieved values | Protosolar Enhancement (\times Solar) |
| H ₂ S below NH ₄ SH | $1.2^{+0.4}_{-0.3} \times 10^{-3}$ | $51.1^{+17.1}_{-12.7}$ |
| NH ₃ below NH ₄ SH | $3.5^{+1.9}_{-2.8} \times 10^{-4}$ | $2.9^{+1.6}_{-2.3}$ |
| CH ₄ | Unconstrained | ... |
| H ₂ S H_{rel} | $46^{+31}_{-34}\%$ | ... |
| PH ₃ | $\leq 4.4 \times 10^{-7}$ | ≤ 0.1 |
| H ₂ State | Unconstrained | ... |
| H ₂ S below all clouds | $1.3^{+0.4}_{-0.3} \times 10^{-3}$ | $53.8^{+18.0}_{-13.4}$ |
| NH ₃ below all clouds | $4.7^{+2.5}_{-3.7} \times 10^{-4}$ | $3.9^{+2.1}_{-3.1}$ |

globally. These upper limits are consistent with the disk-average amount of CH₄ reported by Baines et al. (1995) at 2.2%. However, the 4% deep CH₄ abundance favored by Karkoschka & Tomasko (2011) is similar to our 2σ upper limit. A global dry adiabat permits larger abundances of each condensable, with the CH₄ abundance completely unconstrained. Our CH₄ results may be reconciled with differences in the assumed thermal profiles, as the thermal profile assumed by Karkoschka & Tomasko (2011) is slightly warmer than a wet adiabat.

Our results are consistent with no PH₃ with upper limits of ~ 0.4 – 0.8 ppm, depending on the assumed temperature model. We are completely insensitive to the ortho/para H₂ state.

The relative humidity of H₂S is also unconstrained, apart from 2σ upper limits. As shown in Figure 4, the difference between relative humidities of a few percent or less on the retrieved spectra are minimal when compared to our uncertainties; depleting more and more H₂S has an inconsequential effect on the opacity once enough is removed.

Figures 7 and 8 plot the best-fitting abundance profiles for H₂S and NH₃ between 36°S–12°S and 90°S–66°S assuming wet and dry adiabat temperature profiles, respectively. Five hundred random profiles sampled from the burned-in posterior are also plotted, representing the range of allowable profiles. Brightness temperatures are also plotted, comparing one hundred random retrieved model spectra and data, showing an agreeable fit. A comparison to south polar 2003 VLA data are overplotted as well, showing good agreement. The assumption of a wet adiabat thermal profile does not produce H₂S abundances large enough to be detected by Irwin et al. (2019c; see Figure 7) unless H₂S is supersaturated. For the dry thermal profile, the H₂S-ice cloud forms at higher altitudes and larger H₂S abundances are possible. However, H₂S needs to be fully saturated or supersaturated to reach detectable upper atmosphere abundances.

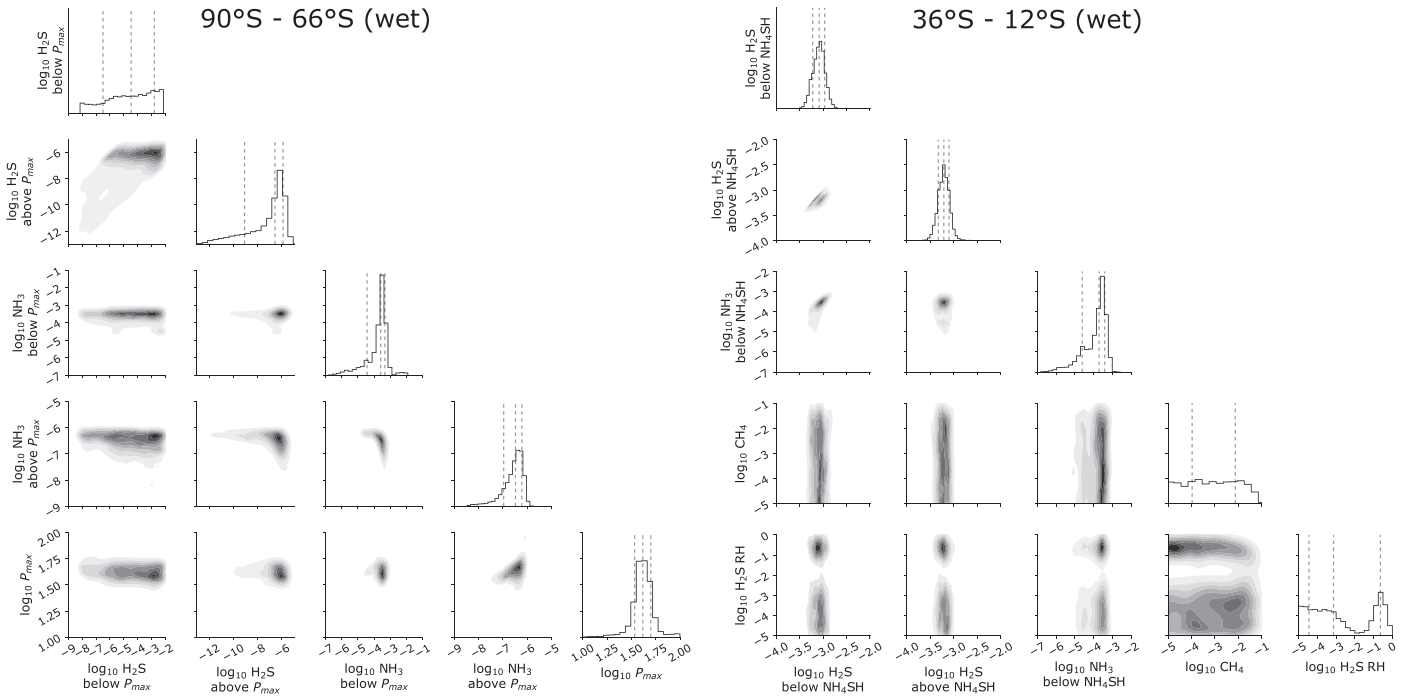


Figure 6. Corner plots of highlighted parameters that control the abundance profiles of the condensibles. Histograms of the retrieved distributions are plotted along diagonals, while the covariance between pairs of parameters are plotted on the off-diagonals. Darker regions on the off-diagonal plots indicate a larger density of retrieved solutions. The 90°S–66°S (left) and 36°S–12°S (right) latitude regions are shown, which both assume a wet adiabat. Dashed vertical lines mark the median and 1 σ bounds.

4.3. Globally Varying Profiles—Mitigating Systematic Uncertainty

One shortcoming of the analysis in the previous section is that the calibration error masks the evident brightness variations across the disk. In this section, we simultaneously model the atmospheric properties matching both the observed brightness temperature within the 36°S–12°S latitudinal band, and the observed temperature differences between 36°S and 12°S and other latitudes. This approach reveals the cause of spatial trends in the brightness temperature. The new likelihood function to maximize is:

$$\ln p(T_b | \nu, \theta, \sigma) = -0.5 \sum_{v_n} \left[\left(\frac{T_{b,n} - T_{b,m}}{\sigma_n} \right)^2 + \log(2\pi\sigma_n^2) \right] - 0.5 \sum_{v_n} \left[\left(\frac{\Delta T_{b,n} - \Delta T_{b,m}}{\sigma_{\Delta,n}} \right)^2 + \log(2\pi\sigma_{\Delta,n}^2) \right]. \quad (4)$$

The first sum on the right side is the same as Equation (1) and represents the fit to the observed brightness temperature at 36°S–12°S with errors dominated by systematic calibration. The second sum represents the brightness temperature difference between 36°S–12°S and the other latitudinal band:

$$\Delta T_b = T_{36^{\circ}\text{S}-12^{\circ}\text{S}} - T_{\text{other latitude}}. \quad (5)$$

Errors in the temperature variation between latitudes at the same wavelength are mainly due to random fluctuations. The uncertainty σ_{Δ} is:

$$\sigma_{\Delta} = (\Delta T_b \cdot 0.05)^2 + \sigma_{\text{RMS}_1}^2 + \sigma_{\text{RMS}_2}^2 + \sigma_{\text{PSF}}^2. \quad (6)$$

The first term on the right side is the difference in brightness temperature between the reference and modeled latitude band times the 5% calibration error. The term σ_{RMS} is the random error on the sky divided by the square root of the number of beams that fit within the reference and modeled latitude bands.

The deep abundances of H₂S, NH₃, and CH₄ are allowed to vary for each pair of latitudes. Moreover, H₂S may either subsaturate or supersaturate. H₂S may be supersaturated up to a pressure P_{ss} . At altitudes shallower than P_{ss} , the H₂S profile follows the saturation curve with 100% relative humidity. At the south polar cap, the abundances of H₂S and NH₃ at pressures shallower than P_{mix} are also allowed to vary, as in the previous section. We assume no PH₃ and fully intermediate H₂ at all latitudes as we do not expect to be sensitive to these parameters given our prior findings (Table 6).

Tables 7 and 8 list the best-fitting values for 16/50/84th uncertainties for constrained parameters assuming a global wet and dry adiabat, respectively. Figures 9 and 10 plot randomly sampled and the best-fitting retrieved trace gas profiles and residual spectra ΔT . We obtain good agreement between the observed and modeled temperature differences. Moreover, the retrieved parameters for the 36°S–12°S band are consistent between model runs to within uncertainties, indicating this approach is self-consistent.

These results show global variability in Neptune’s NH₃ and H₂S abundances. NH₃, although overall very much depleted due to the formation of NH₄SH, is enriched at the south polar cap above P_{mix} relative to the rest of the planet. A globally uniform H₂S abundance below NH₄SH formation is consistent with our results. However, above NH₄SH formation, the H₂S abundance decreases poleward, mirroring brightness temperature increases poleward (Figure 1). Differences in the H₂S relative humidity cause the apparent brightness variations in the

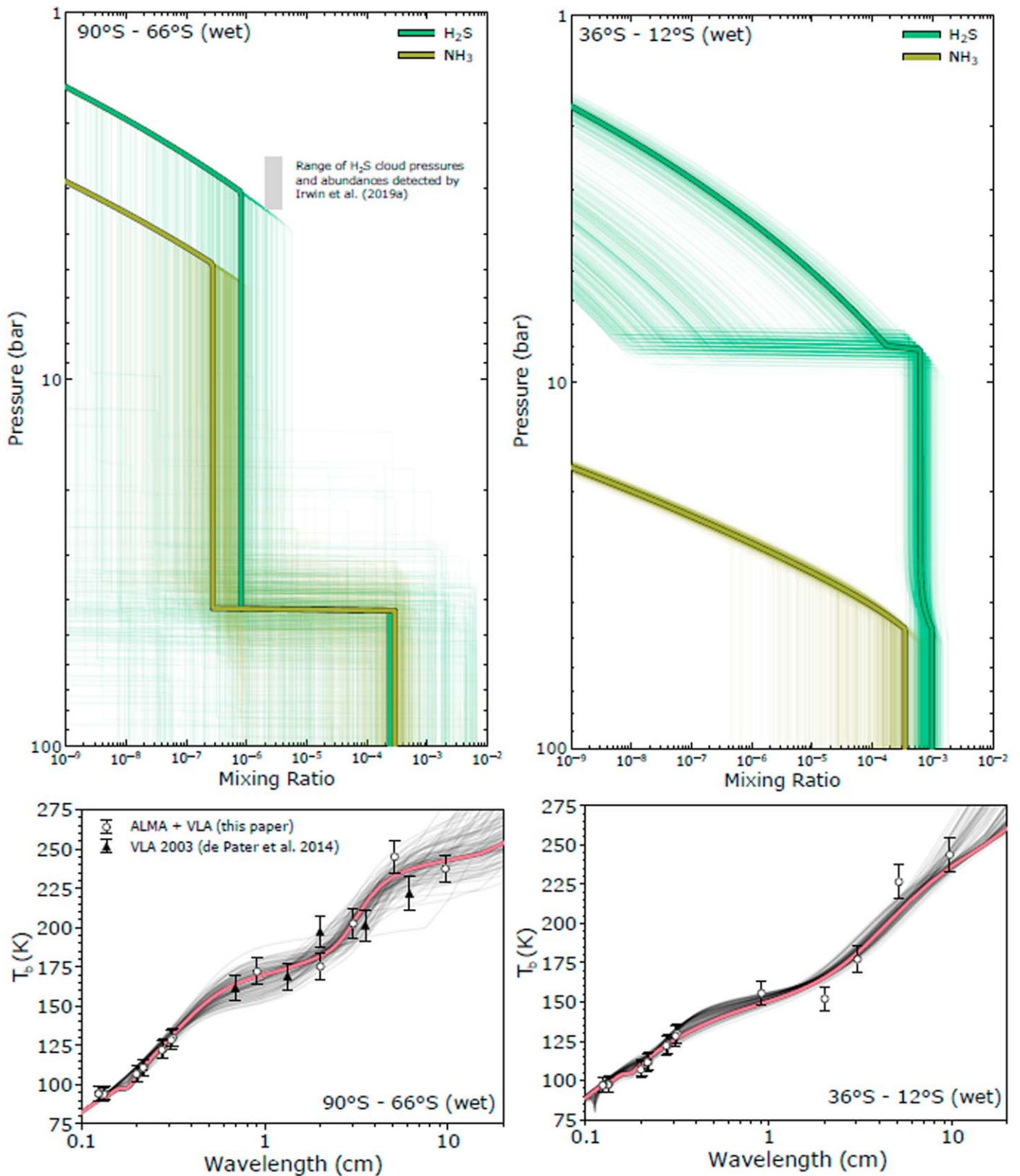


Figure 7. As in Figure 5, except at 90°S–66°S (left) and 36°S–12°S (right), assuming a global wet adiabat. Thick green and yellow lines plot the best-fitting H₂S and NH₃ profiles, respectively. The thick red line in the brightness spectra correspond to the best-fitting profiles. The gray box indicates the range of possible cloud top pressures and H₂S abundances detected by Irwin et al. (2019c) over the south polar cap, showing that H₂S is only detectable in our model at 100% or greater relative humidity.

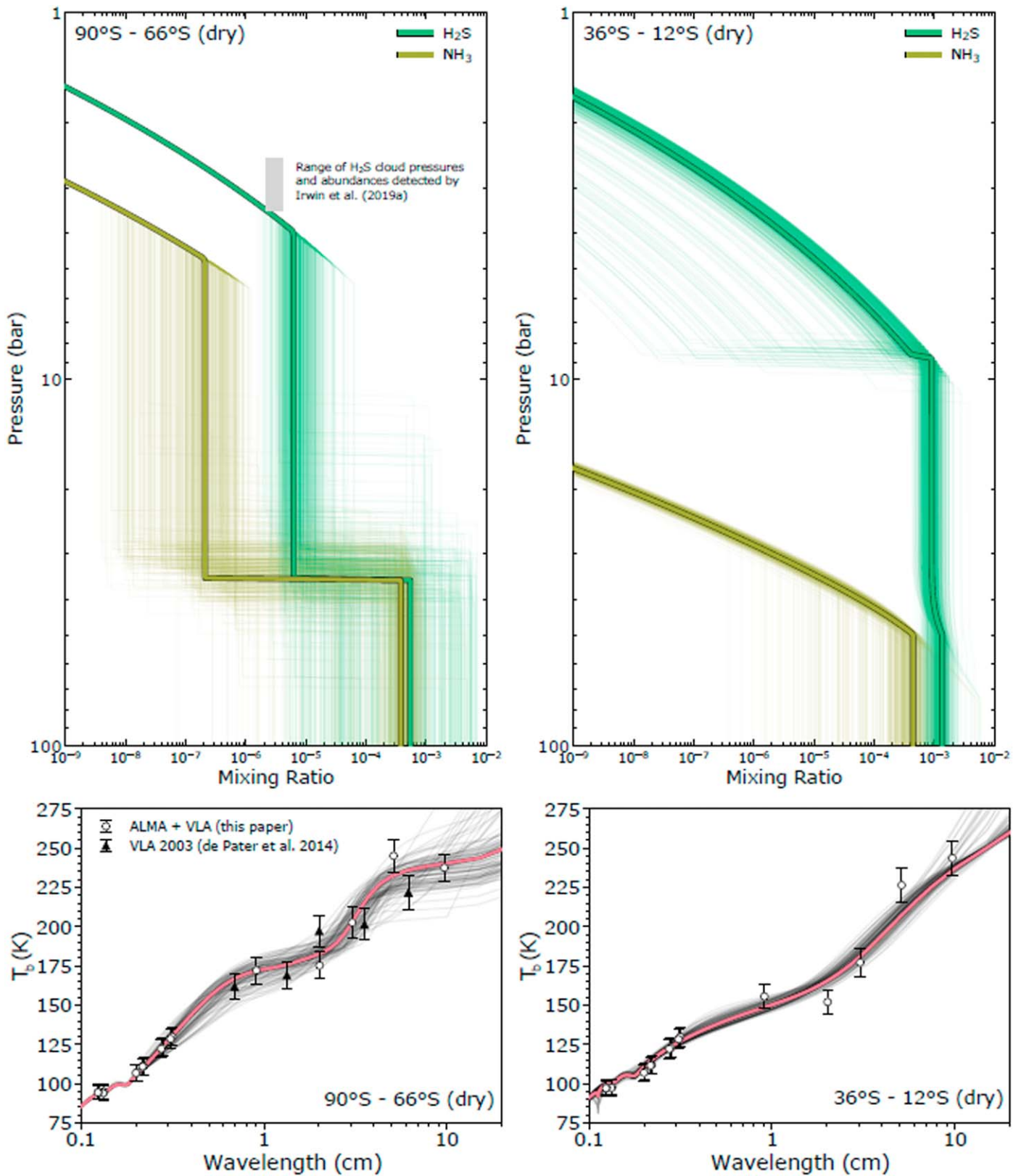


Figure 8. As in Figure 7, except assuming a global dry adiabat.

short-wavelength maps, which probe the H₂S-ice cloud and are coldest and darkest at 36°S–12°S and 4°N–20°N. These regions are also where supersaturated H₂S is needed in order to fit the observed temperature variations. This discussion is visually summarized in Figure 11, which plots the probability

density of the retrieved H₂S mixing ratio in each latitude band relative to that obtained for 36°S–12°S in the simultaneous fit. These plots demonstrate the magnitude and significance of these variations at the three pressure regimes discussed: below NH₄SH formation (100 bar), above H₂S-ice formation (5 bar),

Table 7

MCMC Retrieved Parameters for the Simultaneous Latitudinal Band Fitting, Matching the Observed Brightness Temperature Variations at a Given Latitude Band Compared To That at 36°S–12°S, Assuming a Global Wet Adiabatic

| Latitude Bin: | 90°S–66°S | 66°S–50°S | 50°S–36°S | 12°S–4°N | 4°N–20°N |
|---|--|------------------------------------|------------------------------------|------------------------------------|------------------------------------|
| Free Parameter | Retrieved values—global wet adiabat | | | | |
| H ₂ S below NH ₄ SH | $9.5^{+2.5}_{-2.3} \times 10^{-4}$ | $7.7^{+2.1}_{-1.3} \times 10^{-4}$ | $8.0^{+1.3}_{-1.6} \times 10^{-4}$ | $8.5^{+1.4}_{-1.3} \times 10^{-4}$ | $9.2^{+2.4}_{-1.7} \times 10^{-4}$ |
| NH ₃ below NH ₄ SH | $0.9^{+0.5}_{-0.4} \times 10^{-4}$ | $2.7^{+2.2}_{-1.1} \times 10^{-4}$ | $3.1^{+1.3}_{-1.5} \times 10^{-4}$ | $2.6^{+1.0}_{-1.2} \times 10^{-4}$ | $1.7^{+1.6}_{-1.3} \times 10^{-4}$ |
| CH ₄ | $\leq 0.5 \times 10^{-2}$ | $\leq 0.6 \times 10^{-2}$ | $\leq 0.6 \times 10^{-2}$ | $\leq 0.8 \times 10^{-2}$ | $\leq 0.5 \times 10^{-2}$ |
| H ₂ S H_{rel} (%) | 18^{+13}_{-11} | 49^{+5}_{-3} | 80^{+5}_{-3} | 76^{+8}_{-3} | ≥ 70 |
| P_{ss} (bar) | not supersat. | not supersat. | not supersat. | not supersat. | ≥ 7.9 |
| P_{mix} (bar) | 38^{+3}_{-3} | ... | ... | ... | ... |
| H ₂ S above P_{mix} | $1.4^{+0.6}_{-0.3} \times 10^{-5}$ | ... | ... | ... | ... |
| NH ₃ above P_{mix} | $9.0^{+9.0}_{-3.9} \times 10^{-7}$ | ... | ... | ... | ... |
| Free Parameter | Corresponding 36°S–12°S retrieved values | | | | |
| H ₂ S below NH ₄ SH | $7.9^{+1.1}_{-0.9} \times 10^{-4}$ | $9.3^{+1.5}_{-1.6} \times 10^{-4}$ | $7.5^{+2.1}_{-1.3} \times 10^{-4}$ | $8.1^{+1.7}_{-1.3} \times 10^{-4}$ | $9.1^{+1.9}_{-1.3} \times 10^{-4}$ |
| NH ₃ below NH ₄ SH | $2.9^{+1.1}_{-1.4} \times 10^{-4}$ | $2.1^{+1.9}_{-1.3} \times 10^{-4}$ | $2.7^{+1.8}_{-1.3} \times 10^{-4}$ | $2.8^{+1.6}_{-1.4} \times 10^{-4}$ | $1.3^{+1.4}_{-1.0} \times 10^{-4}$ |
| CH ₄ | $\leq 4.0 \times 10^{-2}$ | $\leq 1.3 \times 10^{-2}$ | $\leq 0.9 \times 10^{-2}$ | $\leq 1.3 \times 10^{-2}$ | $\leq 0.8 \times 10^{-2}$ |
| P_{ss} (bar) | ≥ 6.4 | ≥ 7.3 | $7.2^{+0.3}_{-0.4}$ | $6.9^{+0.3}_{-0.3}$ | $8.2^{+0.5}_{-0.4}$ |
| H ₂ S H_{rel} (%) | ≥ 48 | ≥ 90 | not subsat. | not subsat. | not subsat. |
| σ_{PSF} (%) | ≤ 6 | ≤ 1 | ≤ 2 | ≤ 2 | ≤ 6 |

Note. A column in the top table lists the values of retrieved parameters at the given latitude band, while the corresponding column in the bottom table lists those obtained at 36°S–12°S in the simultaneous fit (Equation (4)). Free parameters marked with a “...” were not allowed to vary at that latitude band. The terms “not supersat.” and “not subsat.” mean that supersaturated and subsaturated H₂S were not obtained in any final retrievals, respectively. The listed values are the 50th percentile of the posterior distributions with the error bars corresponding to the 16th and 84th percentiles, i.e., the 1 σ uncertainties. Parameters for which the 16th and 84th percentiles vary by more than one order of magnitude have the 2.5th/97.5th percentile value listed instead, representing the 2 σ lower/upper limit. If both supersaturated and subsaturated H₂S are possible in a latitude band, the 2 σ limit is listed for both P_{ss} and H₂S H_{rel} .

Table 8

As in Table 7, but Assuming a Global Dry Adiabatic

| Latitude Bin: | 90°S–66°S | 66°S–50°S | 50°S–36°S | 12°S–4°N | 4°N–20°N |
|---|--|------------------------------------|------------------------------------|------------------------------------|------------------------------------|
| Free Parameter | Retrieved values—global dry adiabat | | | | |
| H ₂ S below NH ₄ SH | $\leq 5.7 \times 10^{-3}$ | $1.2^{+0.4}_{-0.3} \times 10^{-3}$ | $1.0^{+0.3}_{-0.1} \times 10^{-3}$ | $1.0^{+0.5}_{-0.3} \times 10^{-3}$ | $1.9^{+0.5}_{-0.5} \times 10^{-3}$ |
| NH ₃ below NH ₄ SH | $1.7^{+0.9}_{-0.8} \times 10^{-4}$ | $4.8^{+3.3}_{-3.5} \times 10^{-4}$ | $2.2^{+2.3}_{-1.3} \times 10^{-4}$ | $2.8^{+3.3}_{-1.5} \times 10^{-4}$ | $\leq 9.5 \times 10^{-4}$ |
| CH ₄ | $\leq 3.1 \times 10^{-2}$ | $\leq 5.7 \times 10^{-2}$ | $\leq 6.0 \times 10^{-2}$ | $\leq 1.5 \times 10^{-2}$ | $\leq 2.3 \times 10^{-2}$ |
| H ₂ S H_{rel} (%) | 44^{+9}_{-11} | 53^{+4}_{-3} | 78^{+6}_{-4} | 78^{+5}_{-4} | ≥ 61 |
| P_{ss} (bar) | not supersat. | not supersat. | not supersat. | not supersat. | ≥ 8.3 |
| P_{mix} (bar) | 34^{+3}_{-3} | ... | ... | ... | ... |
| H ₂ S above P_{mix} | $\leq 4.5 \times 10^{-4}$ | ... | ... | ... | ... |
| NH ₃ above P_{mix} | $\leq 4.1 \times 10^{-6}$ | ... | ... | ... | ... |
| Free Parameter | Corresponding 36°S–12°S retrieved values | | | | |
| H ₂ S below NH ₄ SH | $7.5^{+2.5}_{-1.7} \times 10^{-4}$ | $1.4^{+0.4}_{-0.5} \times 10^{-3}$ | $1.1^{+0.4}_{-0.4} \times 10^{-3}$ | $9.8^{+2.2}_{-2.3} \times 10^{-4}$ | $1.8^{+0.5}_{-0.4} \times 10^{-3}$ |
| NH ₃ below NH ₄ SH | $0.4^{+1.4}_{-0.2} \times 10^{-4}$ | $3.2^{+3.2}_{-1.8} \times 10^{-4}$ | $1.2^{+3.4}_{-0.6} \times 10^{-4}$ | $3.0^{+4.8}_{-0.8} \times 10^{-4}$ | $3.3^{+4.0}_{-2.3} \times 10^{-4}$ |
| CH ₄ | $\leq 5.3 \times 10^{-2}$ | $\leq 1.6 \times 10^{-2}$ | $\leq 6.7 \times 10^{-2}$ | $\leq 1.5 \times 10^{-2}$ | $\leq 2.7 \times 10^{-2}$ |
| P_{ss} (bar) | $6.2^{+1.0}_{-0.4}$ | $6.9^{+0.7}_{-0.3}$ | ≥ 5.9 | $6.1^{+0.3}_{-0.2}$ | ≥ 6.8 |
| H ₂ S H_{rel} (%) | not. subsat. | not. subsat. | ≥ 88 | not subsat. | ≥ 79 |
| σ_{PSF} (%) | ≤ 4 | ≤ 2 | ≤ 1 | ≤ 2 | ≤ 9 |

and in between (20 bar). In the [Appendix](#), we show that latitudinal variations in the thermal profile can only explain the observations if the temperature variations are localized to the H₂S-ice formation pressures and are on the order of ~ 8 K or greater.

A measure of the improvement in the fit between two models is the Deviance Information Criterion (DIC, Spiegelhalter et al. 2002). DIC is defined as:

$$\text{DIC} = \overline{D(\theta)} + \frac{1}{2} \text{Var}(D(\theta)). \quad (7)$$

θ are the free parameters, and $\overline{D(\theta)}$ is the mean deviance of the retrieved parameters, which in this case is the average of the log-likelihood *emcee* probabilities, defined in Equation (4). The second term on the right side is one half the variance of these probabilities.

Information criteria like DIC are typically used when analyzing MCMC results in order to select models that provide a good fit to the data (the first term) and minimize the variance in the retrieved probabilities (the second term) resulting from model complexity. The difference between two DIC values can

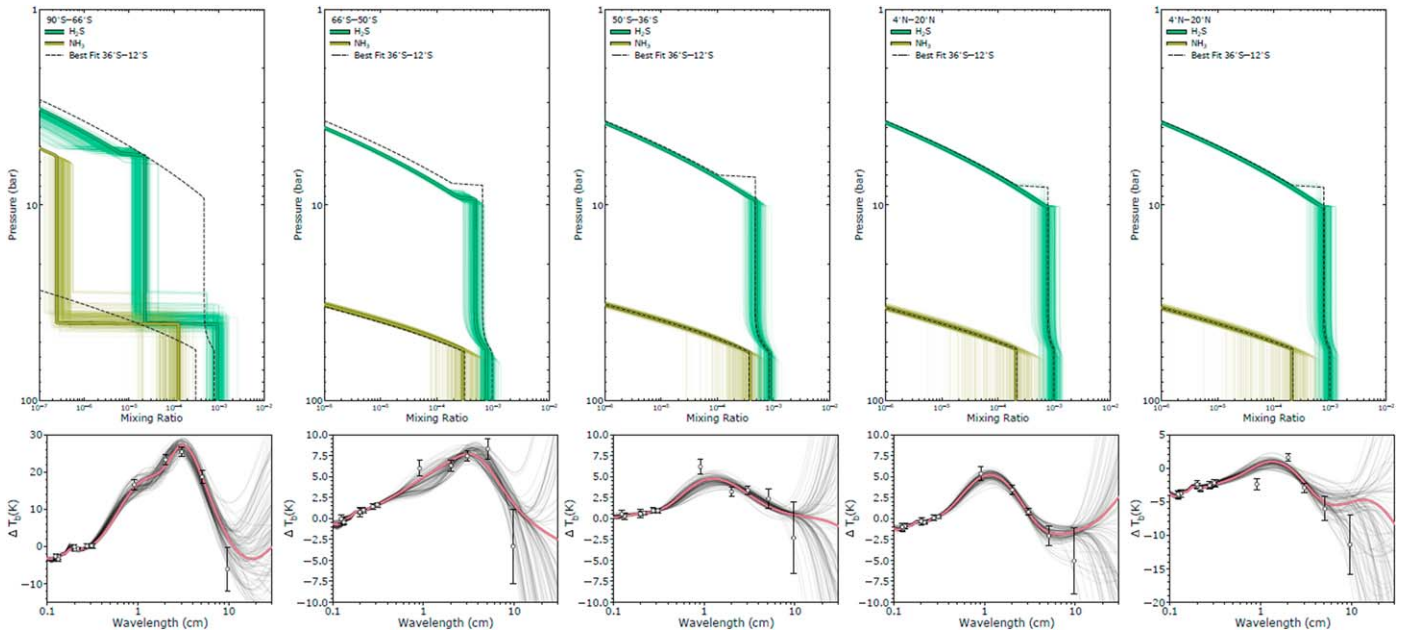


Figure 9. Retrieved abundance profiles (top) and residual brightness temperature spectra (bottom) across Neptune’s disk going northward from left to right, assuming a global wet adiabat. Colors are as in Figure 8 and the dashed black lines denote the best-fitting 36°S–12°S model from the simultaneous fit. Note that these profiles for 36°S–12°S vary from panel to panel as its model parameters are retrieved independently for each simultaneous fit with the given latitude band. However, all are consistent to within the retrieved uncertainty. Good fits to the observed and modeled temperature variations are obtained. The brightness temperature variations, defined as ΔT_b in Equation (5), are plotted in the bottom panels, with the best-fit model plotted in red and 100 random models in black. Positive values indicate that the modeled latitude band is warmer than 36°S–12°S at that wavelength.

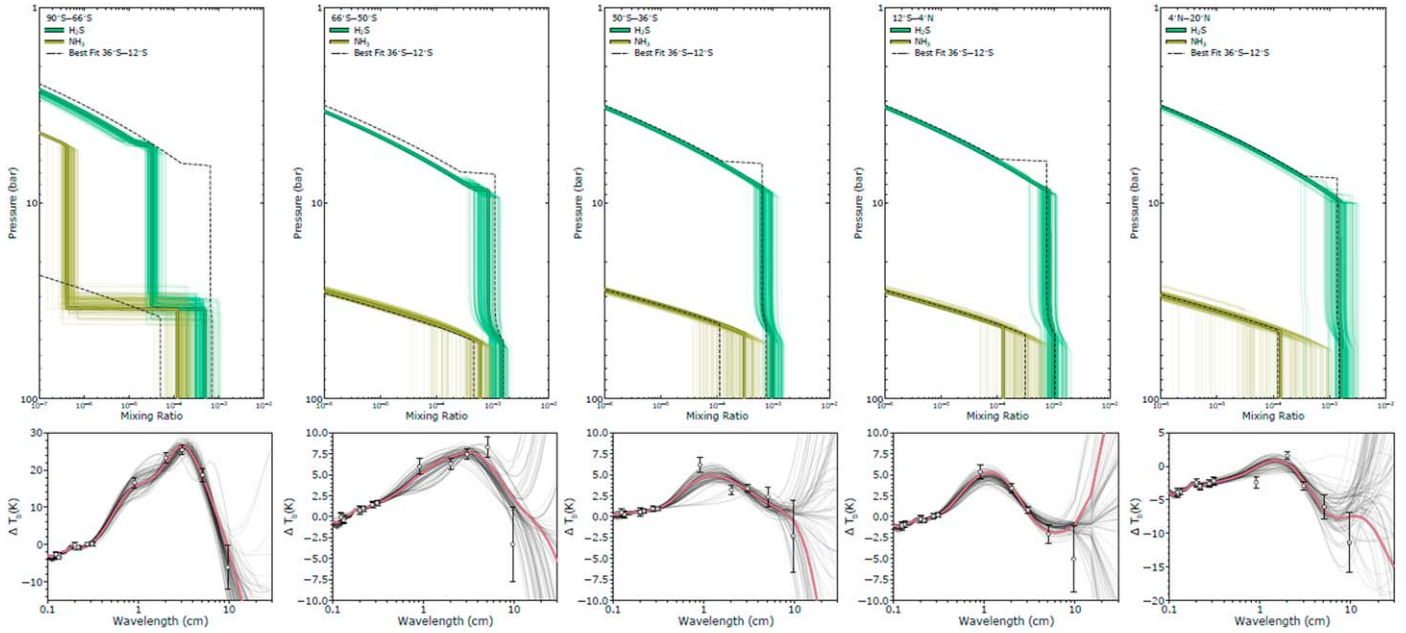


Figure 10. As in Figure 9, but assuming a global dry adiabat.

be used to determine the better model assuming the parameters roughly follow a Gaussian distribution. Differences greater than 10 favor the model with the lower DIC score.

Table 9 lists the DIC score for the global wet and dry adiabat models at each latitude band. The dry adiabat is statistically favored everywhere, apart from 50°S to 36°S where neither thermal profile is favored. We additionally show in Section 2 of the Appendix that when the lapse rate is allowed to vary with the trace gas abundances, the resulting retrieved temperature–

pressure profiles follow a dry adiabat more closely than a wet adiabat.

5. Discussion

Retrievals of Neptune’s microwave spectrum from radiative transfer modeling require an atmosphere dominant in H₂S over NH₃. In every retrieval, all NH₃ is taken up by the formation of the NH₄SH cloud around 50 bar, leaving H₂S to persist and

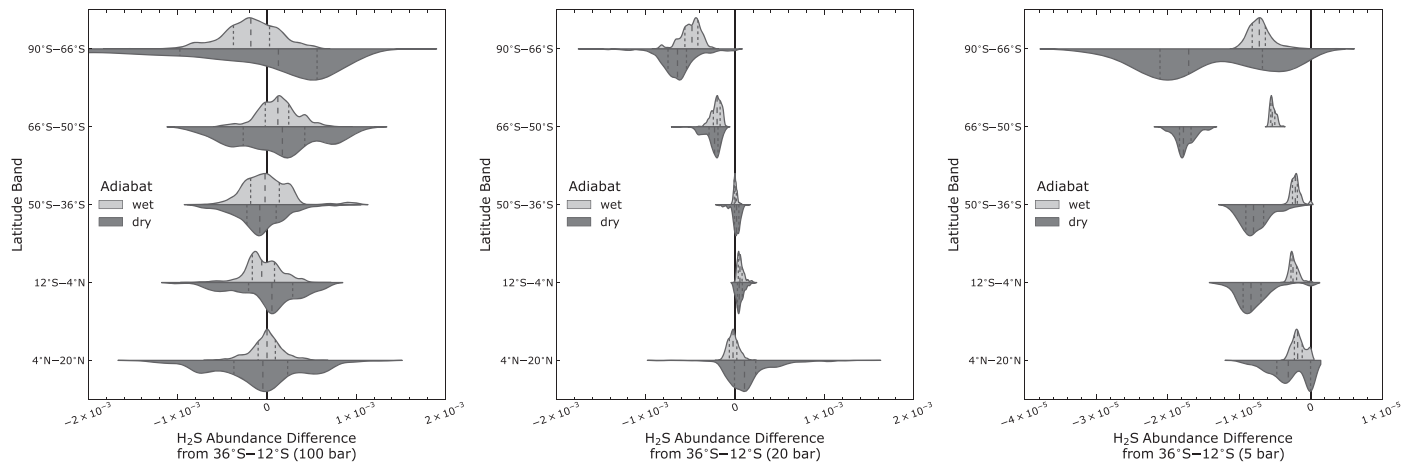


Figure 11. Violin plots showing the probability density of the H_2S mole fraction for different latitude bands relative to values retrieved for the 36°S – 12°S band in the simultaneous fit. Negative values mean the amount of H_2S is higher at 36°S – 12°S . The three panels correspond to three altitudes: 100 bar (left), 20 bar (middle), and 5 bar (right). Distributions are split between the wet and dry thermal models, shaded light and dark, respectively. Dashed lines show the median and upper and lower quartile values.

Table 9
DIC Values for Each Latitude Band Comparison per Global Temperature Profile

| Latitude Bin: | 90°S – 66°S | 66°S – 50°S | 50°S – 36°S | 12°S – 4°N | 4°N – 20°N | Total |
|-------------------|---|---|---|--|--|-------|
| Wet Adiabatic DIC | 177 | 152 | 145 | 134 | 173 | 781 |
| Dry Adiabatic DIC | 151 | 134 | 130 | 116 | 155 | 689 |
| Difference | +26 | +18 | +15 | +18 | +18 | +95 |

Note. Differences larger than 10 statistically favor the model with the lower DIC score, in this case the global dry adiabat.

condense at higher altitudes. The global thermal profile has a moderate impact on the produced H_2S and NH_3 profiles. Below all cloud formation, we obtain H_2S abundances of $8.7^{+2.6}_{-1.7} \times 10^{-4}$ ($37.3^{+15.7}_{-10.3} \times$ protosolar) for a wet adiabat and $1.3^{+0.4}_{-0.3} \times 10^{-3}$ ($53.8^{+18.9}_{-13.4} \times$ protosolar) for a dry adiabat. We are less sensitive to the deep NH_3 abundance as all contribution functions probe at and above the NH_4SH cloud. However, we do find a clear positive correlation between the H_2S and NH_3 abundances: more deep NH_3 requires more deep H_2S . We obtain loose bounds on the NH_3 abundance: $2.5^{+2.7}_{-2.3} \times 10^{-4}$ ($2.1^{+2.3}_{-1.9} \times$ protosolar) for a wet adiabat and $4.7^{+2.5}_{-3.7} \times 10^{-4}$ ($3.9^{+2.1}_{-3.1} \times$ protosolar) for a dry adiabat. Models fitting to the brightness temperature variations between latitude bands statistically favor a globally uniform thermal profile following a dry adiabat.

Using the $\text{H}_2\text{S}/\text{NH}_3$ ratio as a proxy for the S/N, we completely rule out observable S/Ns less than unity. This is in agreement with earlier radio work on Neptune, although we obtain better constraints on these abundances (de Pater et al. 1991, 2014; DeBoer & Steffes 1996; Luszcz-Cook et al. 2013; Tollefson et al. 2019). Sub-unity S/N is also ruled out on Uranus, suggesting some commonality in the formation history of the ice giants (Gulkis et al. 1978; de Pater et al. 1991; de Pater 2018; Molter et al. 2021). However, their true bulk S/N may be much smaller than observed or assumed, due to the potential loss of ammonia in an ionic/superionic water ocean at 20 GPa (Atreya et al. 2019). Indeed, if CO is uplifted into Neptune’s troposphere, it implies that the water content and O/H ratio is several hundred times protosolar (Luszcz-Cook & de Pater 2013). An additional way to explain the absence of N is the preferential delivery of volatiles onto planetesimals via hydrated clathrates (Hersant et al. 2004). In the cold

environment of the outer protoplanetary disk, the N_2 to NH_3 fraction is roughly 10, while S is primarily in the form of H_2S . Both H_2S and NH_3 are readily trapped in hydrated clathrates while N_2 gas is not, meaning the majority of available N will not be swept into the ice giants. The clathrated hydrates hypothesis also implies that the O/H ratio within Uranus and Neptune is at least 100 times protosolar.

The differences in brightness temperature between latitude regions reveal prevalent global variations in the H_2S and NH_3 profiles. Brightness temperature variations between latitude bands were modeled by comparing the retrieved spectra to profiles simultaneously fit to the 36°S – 12°S region. This approach limits the calibration error, placing tight constraints on how the trace gas profiles vary latitudinally.

At the south pole, the data can be fit with a downwelling atmosphere, where air depleted in H_2S and NH_3 species subsides down to a mixing pressure, P_{mix} , below which the atmosphere becomes well mixed and the trace species equal their deep values. The best-fit retrieved H_2S and NH_3 mixing ratios at altitudes above P_{mix} are 4.4×10^{-5} and 4.1×10^{-7} , respectively, for a dry adiabat. This is in broad agreement with south polar models of 2003 VLA data presented in de Pater et al. (2014), whose best-fitting depleted model required 3.5×10^{-5} parts H_2S and 1.2×10^{-8} parts NH_3 above the NH_4SH cloud.

Below NH_4SH formation, our results are consistent with homogenous NH_3 and H_2S . Clear latitudinal trends in the H_2S profile, however, must be present at higher altitudes. Just above NH_4SH cloud formation, the H_2S abundance is highest between around the equator and mid-latitudes and diminishes poleward.

Irwin et al. (2019c) tentatively detected 1–3 ppm H_2S at Neptune’s cloud tops between 2.5 bar and 3.5 bar. Their

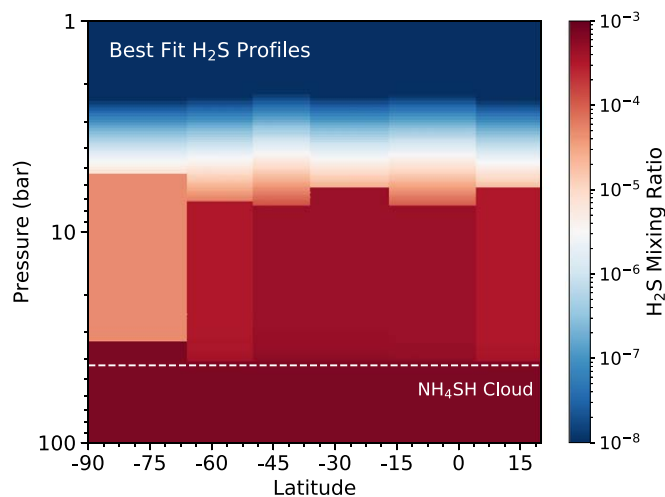


Figure 12. The best-fitting global H_2S profile from MCMC retrievals.

detection is more robust near the south pole than the equator and both their retrieved cloud top pressures and abundances increase toward the south pole. Our results assuming a wet adiabat globally are not consistent with their findings (for instance, see the gray rectangles in Figure 7). The wet thermal profile is about 7 K cooler at 3 bar than the Irwin et al. (2019c) profile. Only our dry adiabat models at the south pole allow H_2S gas abundances close to the values found by Irwin et al. (2019c), as warmer temperatures push the H_2S cloud base to higher altitudes.

Supersaturated H_2S between 36°S and 12°S and possibly between 4°N and 20°N is required to obtain good fits to the observed brightness temperature variations if the thermal profile is fixed globally. Numerous near-infrared works favor a two-layer cloud/haze structure featuring a shallow tenuous upper haze and an opaque cloud deck between 2 bar and 4 bar (Irwin et al. 2014; Luszcz-Cook et al. 2016; Molter et al. 2019). This lower cloud is presumably H_2S -ice, supporting our finding. The ratio of the partial pressure of the condensate in a supersaturated model to the partial pressure of condensate following its saturation curve, ϕ , is a few hundred percent in our H_2S supersaturation model. Similar degrees of supersaturation are expected within ammonia plumes on Jupiter (de Pater et al. 2019). However, on Earth ϕ does not exceed 10% for water (Young 1993). This is because the timescale of cloud formation is very quick in the presence of cloud condensation nuclei (CCN). Little is known about the amount of CCNs available on the gas giants. But, theoretical calculations by Moses et al. (1992) of homogeneous, heterogeneous, and ion-induced nucleation rates produce large values and ranges for ϕ , depending on the species. They find $\phi \geq 3$ –1000 in order for methane and photolyzed hydrocarbon aerosols to form in Neptune’s stratosphere. Neptune may lack substantive amounts of CCN conducive to aerosol formation. Future work should consider both the effect of cloud micro-physics and dynamics on the trace gas distributions within the ice giants.

The above discussion is synthesized in Figure 12, which shows one potential global H_2S profile. For each latitudinal band, we assume the best-fitting H_2S abundances and relative humidities from Table 8. Broadly, these meridional trends in gas abundances are related to the global circulation patterns of the planet.

Warm temperatures within Neptune’s south polar cap are detected at mid-infrared and radio wavelengths. In the mid-infrared, Hammel et al. (2007) observe a warm south pole explained by prevalent ethane and methane emission. Orton et al. (2007) further argue that seasonal warming at the south polar cap may explain the excess of these molecules in the stratosphere; the warm temperatures would overcome the cold-trapping of methane below its condensation point at ~ 1 bar and allow methane to escape upward, diffuse globally, and form ethane via photolysis. Orton et al. (2007) also argue that rising air would be expected given the unexpected high abundances of these species. However, warm temperatures relative to the rest of the planet seen in the mid-infrared thermal emission (Fletcher et al. 2014) and a lack of widespread, persistent cloud coverage in the near-infrared (e.g., de Pater et al. 2014) are more indicative of dry subsiding air. Radio observations, including these, observe high brightness temperatures at Neptune’s south polar cap (Luszcz-Cook et al. 2013; de Pater et al. 2014; Tollefson et al. 2019), which we also interpret as dry, low-opacity, subsiding air. Cloud coverage surrounding the south polar cap and faint, distinct near-infrared clouds located near, but not at, the south pole might be indicative of vigorous convection (Luszcz-Cook et al. 2010), analogous to Saturn’s polar activity (Dyudina et al. 2008; Fletcher et al. 2008). This vigorous convection may be a mechanism to explain all observations across the wavelength spectrum.

The mid-latitudes, defined loosely as between 50°S – 15°S and northward of 15°N , are where Neptune’s brightest and strongest methane cloud activity is observed in the near-infrared (Martin et al. 2012; Fitzpatrick et al. 2014; de Pater et al. 2014; Tollefson et al. 2018). In contrast, the equatorial region is nearly featureless. In addition, the mid-latitudes are colder than the equator and south pole in the mid-infrared (Conrath et al. 1998; Fletcher et al. 2014). Combining these observations, a global circulation pattern is inferred at altitudes shallower than ~ 1 bar (where the near- and mid-infrared probe): cold, enriched methane air rises at the mid-latitudes and travels to the equator and poles, where the methane-depleted air subsides and warms via adiabatic compression. However, this picture is complicated by the relative excess of gaseous CH_4 at the equator, which is more consistent with rising air (Karkoschka & Tomasko 2011; Tollefson et al. 2018; Irwin et al. 2019a). We show in this paper that H_2S is most abundant at the equator and southern mid-latitudes, in line with this meridional trend in CH_4 . At altitudes below methane condensation (~ 1 bar), the aforementioned circulation scheme is, thus, at odds with the retrieved CH_4 and H_2S abundances. Therefore, a more complicated picture of global circulation on Neptune is needed to explain each multiwavelength observation. Fletcher et al. (2020) synthesize decades worth of analysis on the ice giants and argue that vertically stacked circulation cells are necessary to bridge the observed patterns above and below 1 bar on both Uranus and Neptune.

6. Conclusions

We observed Neptune at radio wavelengths with the Very Large Array in five bands between 0.9 cm and 9.7 cm from 2015 September 1–2. The longitude-smeared maps reveal brightness variations across Neptune’s disk. These variations are alternating dark and bright latitudinal bands. Dark (bright) bands are consistent with high (low) opacity sources and cold (warm) brightness temperatures. We model Neptune’s

brightness temperature distribution using the radiative transfer code Radio-BEAR coupled to MCMC, varying the abundance profiles of Neptune’s condensibles to obtain best fits and retrievals to the observed microwave spectra. Models are fit to data from both the VLA presented in this work and 1–3 mm ALMA maps from Tollefson et al. (2019). Combined, these data probe from 1 bar down to >50 bar, where the NH_4SH cloud forms.

1. The assumed thermal profile has a moderate impact on the retrieved H_2S , NH_3 , and CH_4 profiles. A global dry adiabat is preferred over a wet adiabat as a warmer thermal profile is statistically favored in models fitting brightness temperature variations across the disk. All results below are given for the dry adiabat models.
2. The abundances of H_2S and NH_3 below all cloud formation are $1.3_{-0.3}^{+0.4} \times 10^{-3}$ ($53.8_{-13.4}^{+18.9} \times$ protosolar) and $4.7_{-3.7}^{+2.5} \times 10^{-4}$ ($3.9_{-3.1}^{+2.1} \times$ protosolar).
3. The abundance of CH_4 is unconstrained due to its limited impact on the microwave opacity longward of 1 cm. In the millimeter, the CH_4 contribution to the modeled spectra competes with other opacity sources, namely PH_3 , the H_2 state, and the H_2S relative humidity, dulling its signal in the retrievals.
4. The downwelling south polar cap (90°S – 66°S) is consistent with depleted H_2S and NH_3 down to a mixing pressure P_{mix} around the NH_4SH cloud formation: ~ 33 bar. Only when H_2S is fully saturated or supersaturated can retrieved H_2S abundances exceed 1 ppm at 3.5 bar at the south polar cap, as measured by Irwin et al. (2019c). Only our dry adiabat model can produce values at pressures close to those detected.
5. The observed brightness temperature variations between latitude bins are consistent with decreased H_2S above the NH_4SH cloud deck moving away from 36°S to 12°S .
6. The observed brightness temperature variations are more consistent with models supersaturating H_2S between 36°S – 12°S , and possibly 4°N – 20°N , than with models following thermochemical equilibrium with some subsaturation. Models that do not allow H_2S to supersaturate require latitudinal variations in the kinetic temperature on the order of 8 K or greater to fit the data. These variations in the thermal profile are localized to H_2S -ice formation pressures. Future work is needed to decouple the effects of temperature and gas opacity on Neptune’s radio spectrum.
7. We find no spectral evidence of PH_3 . Our retrievals are consistent with a PH_3 2σ upper limit of 0.4 ppm ($\leq 0.1 \times$ protosolar).
8. We cannot constrain the ortho/para H_2 fraction anywhere on Neptune.

Advances in radio astronomy are critical for further constraining the abundance of condensibles in the ice giants. A next generation VLA (ngVLA) would improve the resolution ten-fold at 20 cm if the longest 1000 km baselines are utilized (de Pater et al. 2018; Selina et al. 2018). The resulting high-quality data at long wavelengths would permit a strong constraint on the NH_3 abundance beneath the NH_4SH layer and perhaps even on H_2O . In addition, a five-fold improvement in the sensitivity would mean vastly shorter integration times to achieve an equivalent rms to this work, meaning zonal variations can be detected over a similar observing period

and global maps can be obtained. Juno’s big advantage over ground-based radio observations of Jupiter is that it flies beneath the synchrotron radiation belts that dominate longward of 6 cm. This is not an issue on the ice giants. Moreover, the resolution and sensitivity between the ngVLA and a MWR-like instrument on a potential future Neptune orbiter are quite similar (de Pater et al. 2020).

The decision to include an MWR equivalent on a direct mission to the ice giants will have to weigh whether it competes too heavily with the ground-based capabilities of an optimally running ngVLA. Whatever the choice, it is clear that the ngVLA or a direct mission to the planet are required to improve our maps of Neptune’s trace species and elucidate theories regarding the environment in which Neptune formed and evolved.

This paper makes use of VLA data from program VLA/15A-118. The National Radio Astronomy Observatory (NRAO) is a facility of NSF operated under cooperative agreement by Associated Universities, Inc. VLA data used in this report are available from the NRAO Science Data Archive at <https://archive.nrao.edu/archive/advquery.jsp>.

This paper makes use of the following ALMA data: ADS/JAO.ALMA#2016.1.00859.S. ALMA is a partnership of ESO (representing its member states), NSF (USA) and NINS (Japan), together with NRC (Canada), MOST and ASIAA (Taiwan), and KASI (Republic of Korea), in cooperation with the Republic of Chile. The Joint ALMA Observatory is operated by ESO, AUI/NRAO and NAOJ. The National Radio Astronomy Observatory is a facility of the National Science Foundation operated under cooperative agreement by Associated Universities, Inc.

This research was supported by the National Science Foundation, NSF Grant AST-1615004 to the University of California, Berkeley.

E. Molter was supported in part by NRAO Student Observing Support grant #SOSPA6-006.

Appendix

A.1. Globally Uniform Temperature Profiles

In this section, we address the assumption that the temperature profile is globally uniform at a given pressure level. We first show that this assumption leads to reasonable wind speeds according to the thermal wind equation, then demonstrate that not allowing the trace gas abundances to vary meridionally can result in well-modeled spectra only for nonphysical temperature profiles.

We test the validity of the assumption that the meridional temperature gradient is zero for $P > 1$ bar using an order-of-magnitude comparison. The thermal wind equation relates the vertical wind shear to both the meridional gradient in temperature and composition:

$$2\Omega \sin \theta \frac{du}{dr} = -\frac{g}{r_{\text{eq}}} \left(\frac{1}{T} \frac{dT}{d\theta} + \frac{C}{1 + Cq} \frac{dq}{d\theta} \right). \quad (\text{A1})$$

The term Ω is Neptune’s rotation rate (1×10^{-4} rad s^{-1}), θ is the latitude (rad), u is the zonal wind velocity (m s^{-1}), r is altitude (m), r_{eq} is Neptune’s equatorial radius (2.5×10^7 m), g is Neptune’s gravitational constant (10 m s^{-2}), T is the temperature, q is the molar mass fraction of CH_4 (the most

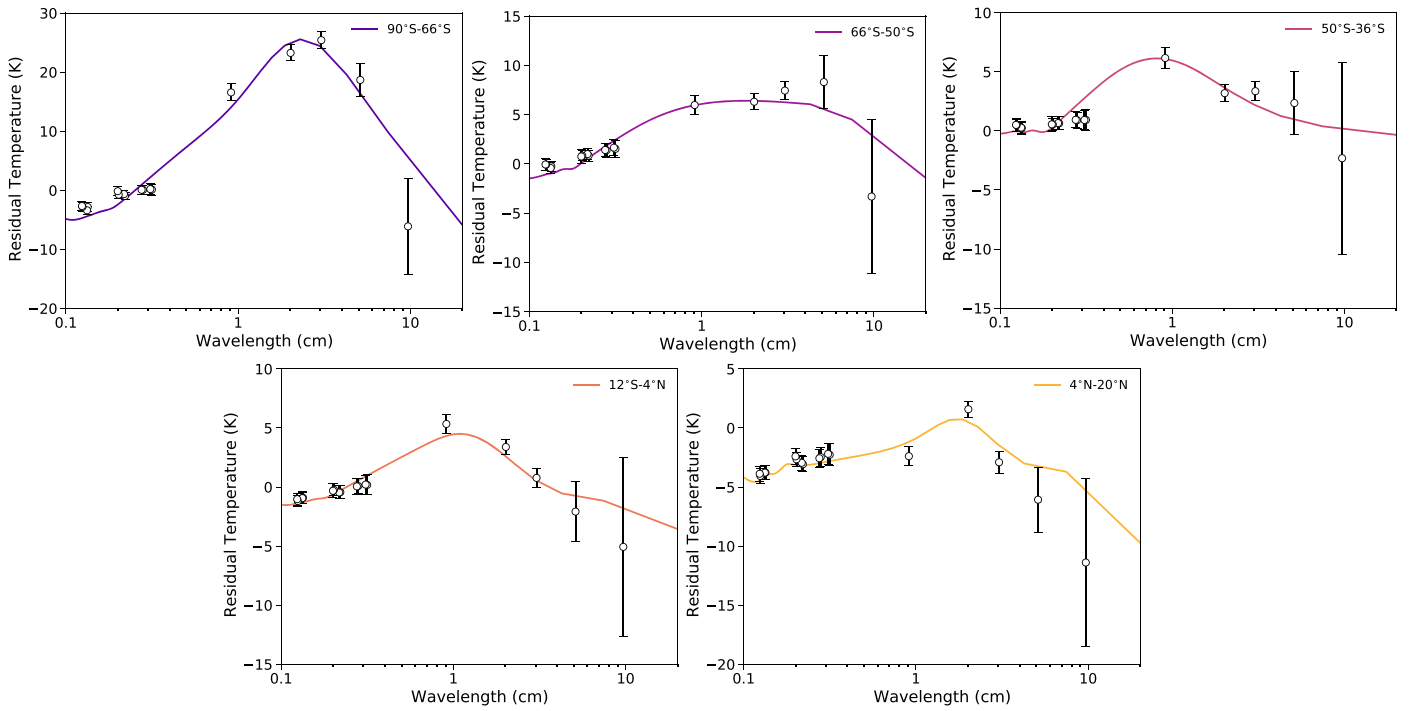


Figure A1. Residual temperatures as a function of latitude, where the observed temperature at 36°S–12°S is subtracted from the temperature at the given latitude band. Colored lines are example model fits to the data assuming a nominal abundance profile and the same colored temperature profile given in Figure A2.

prominent trace gas on Neptune), and $C = (1 - \epsilon)/\epsilon$, where ϵ is the molar mass ratio of CH_4 compared to the ambient atmosphere. For the purpose of this exercise, we assume that the ambient atmosphere consists of H_2 , He, and CH_4 ; H_2S and NH_3 have comparatively smaller abundances than CH_4 and are therefore less important to the compositional term. In addition, $\epsilon \approx 7$ and $C \approx -1$. At the southern mid-latitudes, $\sin \theta \approx -0.5$ and the above equation becomes:

$$-1 \times 10^{-4} \frac{du}{dr} \approx 4 \times 10^{-7} \frac{1}{1-q} \frac{dq}{d\theta}. \quad (\text{A2})$$

From Karkoschka & Tomasko (2011), q is about 0.1 at Neptune’s south pole (≤ 1 –2% mixing ratio) and 0.2 toward the southern mid-latitudes and equator (≥ 2 –4%). So, $dq/d(\theta) \sim +0.1$ at the mid-latitudes for $1 \leq P \leq 3$ bar. Thus, the right side is about 5×10^{-8} and $du/dr \approx -0.5 \text{ m s}^{-1} \text{ km}^{-1}$. The sign and magnitude of this estimate is similar to that of Tollefson et al. (2018), who observed vertical wind shear at Neptune’s equator by tracking near-infrared clouds. Therefore, the thermal wind equation alone cannot rule out the assumption of constant meridional temperatures.

Since the vertical wind shear is relatively unconstrained, especially below 1 bar, meridional kinetic temperature variations are not precluded from a thermal wind analysis. To test this, we estimate what temperature profile is needed to model the observed residual brightness temperatures. We fix the trace gas abundances globally to equal the nominal model (30× solar H_2S , CH_4 , H_2O , and 1× solar NH_3 , with no PH_3 , “intermediate” H_2 , and 100% relative humidity at all cloud formation). Figure A1 plots the observed and modeled temperature variations versus wavelength, meaning a dry adiabat model for 36°S–12°S is subtracted from the model temperature at each other latitude bin. The temperature profiles

used to create these models are plotted in Figure A2. To fit the residual temperatures, two adjustments to the dry adiabatic lapse rate are required. If the kinetic temperature were the sole cause of the brightness temperature variations, then substantial local variations on the order of 8 K or greater are required. Interestingly, these peak around pressures where the H_2S -ice cloud forms (~ 10 bar), suggesting that the natural explanation for meridional brightness variability is due to changes in the H_2S profile altering the microwave opacity.

A.2. Varying Temperature and Trace Gas Abundances with MCMC

In the following, we consider a combination of kinetic temperature and trace gas abundance variations that may explain the observed brightness temperature latitudinal differences. To vary the kinetic temperature in the forward RT model, we allow the lapse rate to vary:

$$\Gamma = -\frac{dT}{dz}. \quad (\text{A3})$$

Assuming hydrostatic equilibrium and the ideal gas law:

$$\Gamma = \rho g \frac{dT}{dP} = \frac{PMg}{RT} \frac{dT}{dP}, \quad (\text{A4})$$

where R is the ideal gas constant, g is the gravitational constant for Neptune, and for each layer P is its pressure, T its kinetic temperature, and M its molecular mass.

The molecular mass of the layer, M , is set by the mole fraction abundance of H_2 , He, and CH_4 , where $[\text{He}]/[\text{H}_2] = 18\%$, in line with infrared results from Burgdorf et al. (2003), and $[\text{CH}_4] = 1.44\%$ (30× protosolar) at altitudes deeper than its condensation pressure. Equation (4) is integrated and solved for $T(P)$. For this work, $T(P)$ is altered by varying the lapse rate at altitudes shallower than a

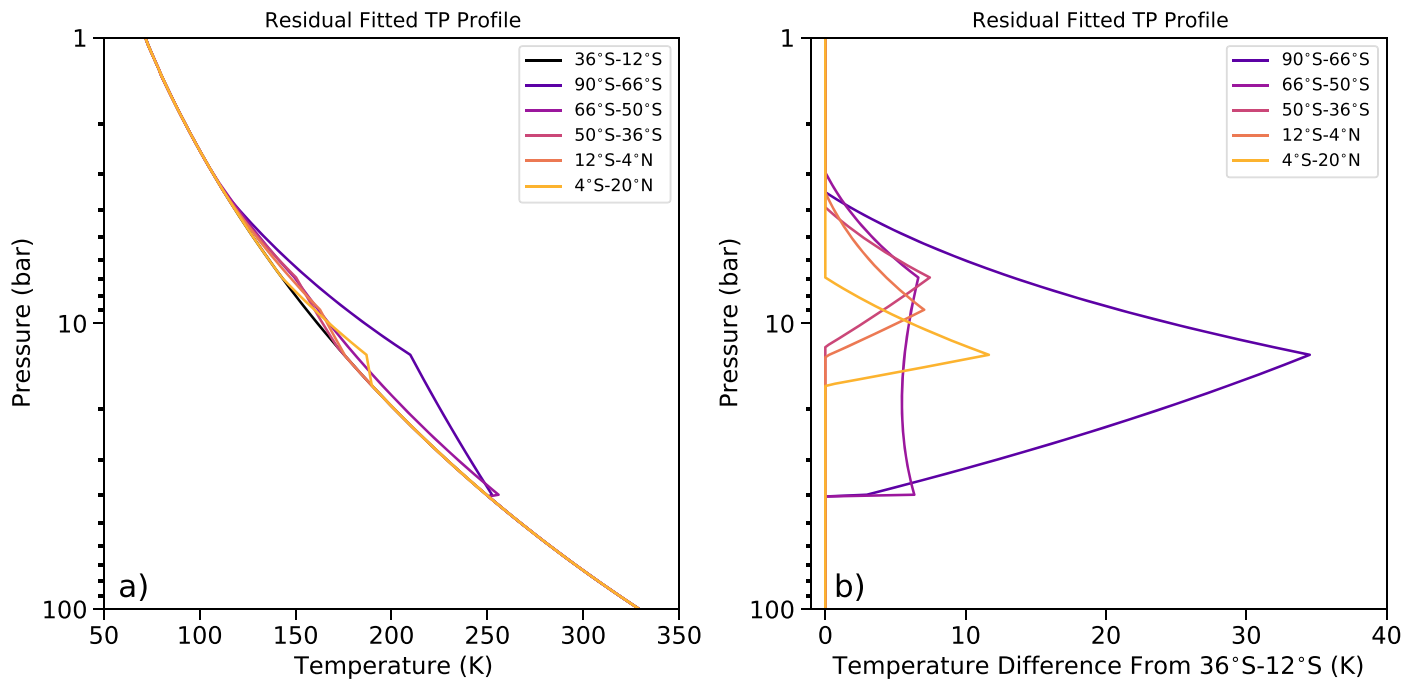


Figure A2. (a) Temperature profiles as a function of latitude (colored lines) producing the residual spectra fits plotted in Figure A1. (b) Residual temperature profile as a function of latitude (colored lines), where the 36°S–12°S dry adiabat profile is subtracted from the temperature at the given latitude band.

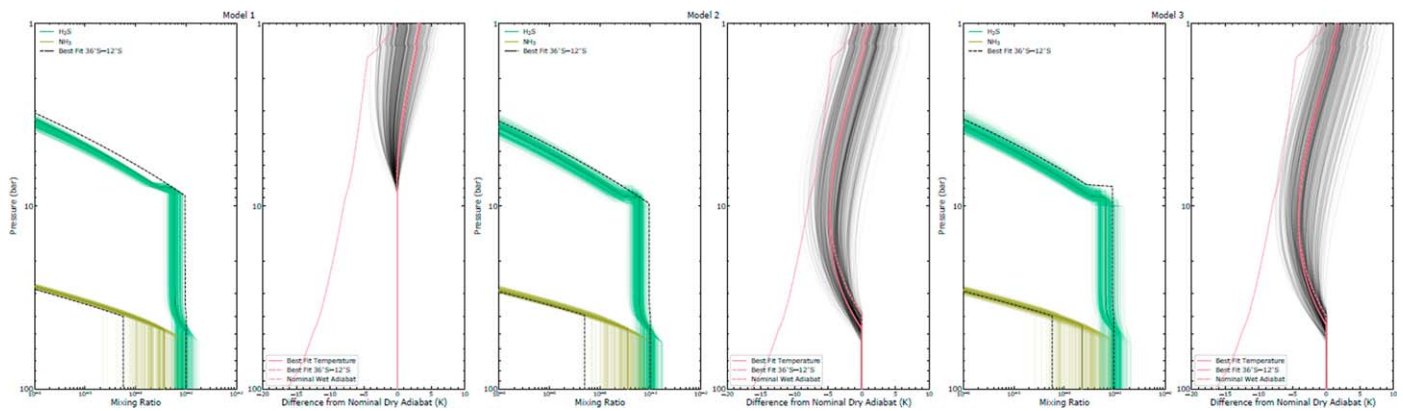


Figure A3. Random retrieved abundance and temperature profiles compared to the nominal dry adiabat at 66°S–50°S for the three types of models considered in this section. The best-fitting profiles at 66°S–50°S are given in bold colored lines, while the best-fitting profiles at 36°S–12°S are given in dashed lines. The temperature profiles are differences from the nominal dry adiabat, with positive values meaning the retrieved model is warmer. The nominal wet adiabat is given in a dotted line for comparison and the difference in shape from the retrievals is due to forcing the temperature at 1 bar to match the Voyager result.

prescribed boundary pressure. At altitudes deeper than this boundary pressure, $T(P)$ is set to the dry adiabat profile used throughout this paper. We run three models fitting ΔT_b between 66°S–50°S and 36°S–12°S. Model 1 sets the boundary pressure at the onset of H₂S-ice formation and does not allow H₂S to supersaturate. Model 2 sets the boundary pressure at the onset of NH₄SH formation and does not allow H₂S to supersaturate. Model 3 sets the boundary pressure at the onset of NH₄SH formation and *does* allow H₂S to supersaturate. Both the lapse rate and condensable profiles are varied independently between latitude bands.

Figures A3 and A4 plot the retrieved gas and temperature profiles and their corresponding residual spectra, respectively, for each of the three models. Table A1 lists the retrieved model parameters, showing that similar NH₃ and H₂S profiles are obtained regardless of the chosen boundary pressure, where the lapse rate begins to vary. Figure A5 plots the χ^2 goodness-of-fit

as a function of wavelength for the best-fitting spectra in each of the three models considered. Only when supersaturated is allowed (model 3) can a good fit be obtained at 0.9 cm. Allowing latitudinal temperature variations without H₂S supersaturation (models 1 and 2) cannot explain all the observed data. In fact, the retrieved latitudinal differences in the kinetic temperature are consistent with zero, as shown in Figure A6. While the 0.9 cm datum is just one point of evidence in favor of supersaturated H₂S, it cannot be explained away by an error in calibration, as discussed in Section 4.3. Figure A3 also shows that the retrieved temperature–pressure profiles are consistent with a dry adiabat, while few retrievals follow the lapse rate of a wet adiabat, consistent with the findings in Section 4.2. We therefore conclude that latitudinal variations in the opacity due to the condensable species are the cause of Neptune’s observed brightness temperature distribution, and the current fitting favors supersaturation of H₂S at the coldest latitudes.

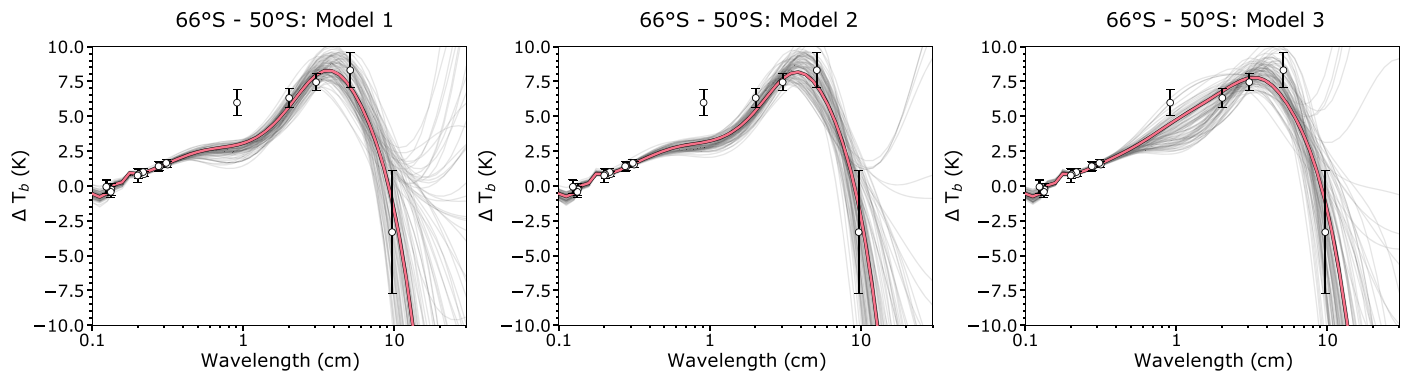


Figure A4. Random retrieved model spectra fitting the observed ΔT_b between 66°S – 50°S and 36°S – 12°S for the three types of models considered in this section. Only model 3, which allows H_2S supersaturation at its ice cloud, provides a good fit to the data at 0.9 cm.

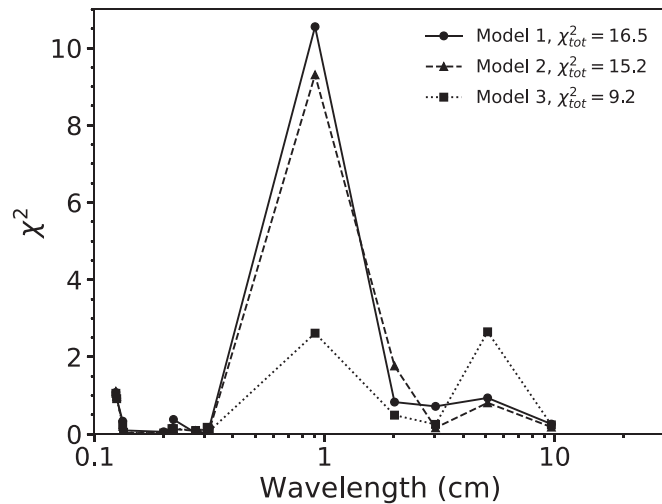


Figure A5. The χ^2 goodness-of-fit vs. wavelength corresponding to the best-fitting residual spectra ΔT_b given in Figure A4, showing that a good fit is achieved everywhere only when H_2S is allowed to supersaturate (model 3). Varying temperature without allowing supersaturation (models 1 and 2) does not produce a good fit at the 0.9 cm data point. The total χ^2 for each model is given in the plot legend.

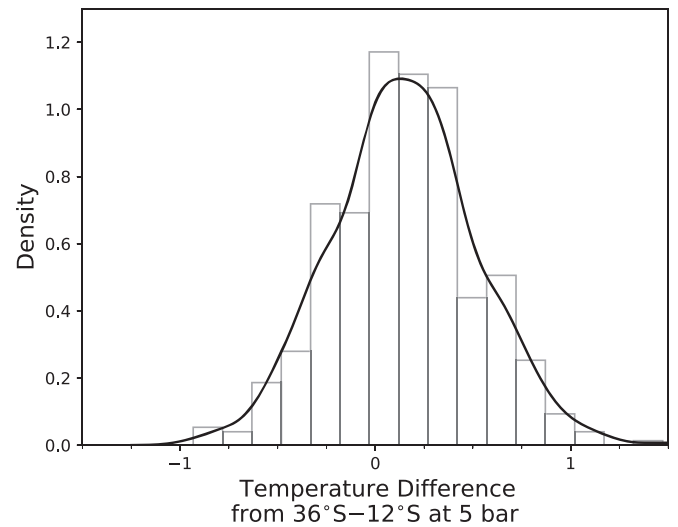


Figure A6. Distribution of retrieved kinetic temperature differences between 66°S – 50°S and 36°S – 12°S at 5 bar for model 3. Differences are consistent with zero and are no larger than 1 K.

Table A1

Retrieved Parameters for Each of the Three Models Considered in This Section

| Latitude Bin: | 66°S – 50°S | 36°S – 12°S |
|---|---|---|
| Free Parameter | Retrieved values—Model 1 | |
| H_2S below NH_4SH | $0.9^{+0.3}_{-0.2} \times 10^{-3}$ | $1.1^{+0.3}_{-0.2} \times 10^{-3}$ |
| NH_3 below NH_4SH | $2.6^{+2.8}_{-1.3} \times 10^{-4}$ | $0.6^{+2.5}_{-0.3} \times 10^{-4}$ |
| H_2S H_{rel} (%) | 48^{+3}_{-6} | 91^{+7}_{-14} |
| Γ (K km^{-1}) | $1.17^{+0.04}_{-0.06}$ | $1.17^{+0.05}_{-0.05}$ |
| Free Parameter | Retrieved values—Model 2 | |
| H_2S below NH_4SH | $1.0^{+0.2}_{-0.3} \times 10^{-3}$ | $1.0^{+0.2}_{-0.2} \times 10^{-3}$ |
| NH_3 below NH_4SH | $3.3^{+2.9}_{-1.8} \times 10^{-4}$ | $0.4^{+1.0}_{-0.3} \times 10^{-4}$ |
| H_2S H_{rel} (%) | 44^{+5}_{-6} | 92^{+6}_{-13} |
| Γ (K km^{-1}) | $1.11^{+0.03}_{-0.02}$ | $1.12^{+0.03}_{-0.03}$ |
| Free Parameter | Retrieved values—Model 3 | |
| H_2S below NH_4SH | $1.0^{+0.3}_{-0.3} \times 10^{-3}$ | $1.1^{+0.3}_{-0.3} \times 10^{-3}$ |
| NH_3 below NH_4SH | $2.5^{+2.7}_{-1.7} \times 10^{-4}$ | $0.5^{+1.8}_{-0.4} \times 10^{-4}$ |
| H_2S H_{rel} (%) | 51^{+4}_{-6} | ≥ 72 |
| P_{ss} (bar) | ... | ≥ 6.8 |
| Γ (K km^{-1}) | $1.11^{+0.02}_{-0.03}$ | $1.12^{+0.02}_{-0.04}$ |

ORCID iDs

Joshua Tollefson <https://orcid.org/0000-0003-2344-634X>
 Imke de Pater <https://orcid.org/0000-0002-4278-3168>
 Edward M. Molter <https://orcid.org/0000-0003-3799-9033>
 Robert J. Sault <https://orcid.org/0000-0001-9209-7716>
 Bryan J. Butler <https://orcid.org/0000-0002-5344-820X>
 Statia Luszcz-Cook <https://orcid.org/0000-0001-9867-9119>
 David DeBoer <https://orcid.org/0000-0003-3197-2294>

References

- Asplund, M., Grevesse, N., Sauval, A. J., & Scott, P. 2009, *ARA&A*, **47**, 481
 Atreya, S. K., Hofstadter, M. D., Reh, K. R., et al. 2019, *AcAau*, **162**, 266
 Atreya, S. K., & Wong, A. 2005, *SSRV*, **116**, 121
 Baines, K. H., Mickelson, M. E., Larson, L. E., & Ferguson, D. W. 1995, *Icar*, **114**, 328
 Burgdorf, M., Orton, G. S., Davis, G. R., et al. 2003, *Icar*, **164**, 244
 Conrath, B., Gierasch, P., & Ustinov, E. A. 1998, *Icar*, **135**, 501
 DeBoer, D. R., & Steffes, P. G. 1996, *Icar*, **123**, 324
 de Kleer, K., Luszcz-Cook, S., de Pater, I., et al. 2015, *Icar*, **256**, 120
 de Pater, I. 2018, *NatAs*, **2**, 364
 de Pater, I., Butler, B., Sault, R., et al. 2018, Science with a Next Generation Very Large Array: Potential for Solar System Science with the ngVLA (San Francisco, CA: ASP)
 de Pater, I., DeBoer, D., & Marley, M. 2005, *Icar*, **173**, 425
 de Pater, I., Fletcher, L. N., Luszcz-Cook, S., et al. 2014, *Icar*, **237**, 211
 de Pater, I., & Massie, S. T. 1985, *Icar*, **62**, 143

- de Pater, I., & Mitchell, D. L. 1993, *JGRE*, **98**, 5471
- de Pater, I., Moeckel, C., Tollefson, J., et al. 2020, Prospects to study the Ice Giants with the ngVLA, Planetary Science and Astrobiological Decadal Survey 2023–2032, 53, 063, <https://baas.aas.org/pub/2021n4i063/release/1>
- de Pater, I., Romani, P. N., & Atreya, S. K. 1991, *Icar*, **91**, 220
- de Pater, I., Sault, R., Wong, M. H., et al. 2019, *Icar*, **322**, 168
- Dyudina, U. A., Ingersoll, A. P., Ewald, S. P., et al. 2008, *Sci*, **319**, 1801
- Fegley, B., Jr+, & Prinn, R. G. 1986, *ApJ*, **307**, 852
- Fitzpatrick, P. J., de Pater, I., Luszcz-Cook, S., Wong, M. H., & Hammel, H. B. 2014, *Ap&SS*, **350**, 65
- Fletcher, L. N., de Pater, I., Orton, G. S., et al. 2014, *Icar*, **231**, 146
- Fletcher, L. N., de Pater, I., Orton, G. S., et al. 2020, *SSRv*, **216**, 21
- Fletcher, L. N., Irwin, P. G. J., Orton, G. S., et al. 2008, *Sci*, **319**, 79
- Fletcher, L. N., Orton, S. G., Teanby, N. A., et al. 2009, *Icar*, **202**, 543
- Foreman-Mackey, D., Hogg, D. W., Lang, D., & Goodman, J. 2013, *PASP*, **125**, 306
- Goodman, J., & Weare, J. 2010, *Commun. Appl. Math. Comput. Sci*, **5**, 65
- Gulkis, S., Janssen, M. A., & Olson, E. T. 1978, *Icar*, **34**, 10
- Hammel, H. B., Sitko, M. L., Lynch, D. K., et al. 2007, *AJ*, **134**, 637
- Hersant, F., Gautier, D., & Lunine, J. I. 2004, *P&SS*, **52**, 623
- Hofstadter, M., Simon, A., Atreya, S., et al. 2019, *P&SS*, **177**, 104680
- Hueso, R., & Sánchez-Lavega, A. 2019, *SSRv*, **215**, 52
- Irwin, P. G., Lellouch, E., de Bergh, C., et al. 2014, *Icar*, **227**, 37
- Irwin, P. G., Toledo, D., Ashwin, B. S., et al. 2019a, *Icar*, **331**, 69
- Irwin, P. G., Toledo, D., Garland, R., et al. 2019b, *NatAs*, **2**, 420
- Irwin, P. G., Toledo, D., Garland, R., et al. 2019c, *Icar*, **321**, 550
- Janssen, M. A., Oswald, J. E., Brown, S. T., et al. 2017, *SSRv*, **213**, 139
- Karkoschka, E., & Tomasko, M. G. 2011, *Icar*, **211**, 780
- Lewis, J. S. 1969, *Icar*, **10**, 365
- Lindal, G. F. 1992, *AJ*, **103**, 967
- Luszcz-Cook, S., de Kleer, K., de Pater, I., Ádámkóvics, M., & Hammel, H. 2016, *Icar*, **276**, 52
- Luszcz-Cook, S., & de Pater, I. 2013, *Icar*, **222**, 379
- Luszcz-Cook, S., de Pater, I., Ádámkóvics, M., et al. 2010, *Icar*, **208**, 938
- Luszcz-Cook, S., de Pater, I., & Wright, M. 2013, *Icar*, **226**, 437
- Martin, S. C., de Pater, I., & Marcus, P. 2012, *Ap&SS*, **337**, 65
- Massie, S. T., & Hunten, D. M. 1982, *Icar*, **49**, 213
- Molter, E., de Pater, I., Luszcz-Cook, S., et al. 2019, *Icar*, **321**, 324
- Molter, E., de Pater, I., Luszcz-Cook, S., et al. 2021, *PSJ*, **2**, 3
- Moses, J. I., Allen, M., & Yung, Y. K. 1992, *Icar*, **99**, 318
- Orton, G. S., Encrenaz, T., Leyrat, C., Puetter, R., & Friedson, A. J. 2007, *A&A*, **473**, L5
- Rymer, A., Runyon, K., Clyde, B., et al. 2020, Neptune Odyssey Flagship Concept to the Neptune-Triton System, Planetary Science and Astrobiological Decadal Survey 2023–2032, <https://science.nasa.gov/science-red/s3fs-public/atoms/files/Neptune%20Odyssey.pdf>
- Sault, R. J., Teuben, P. J., & Wright, M. C. H. 1995, in ASP Conf. Ser. 77, Astronomical Data Analysis Software and Systems IV, ed. R. Shaw, H. E. Payne, & J. J. E. Hayes (San Francisco, CA: ASP), 433
- Selina, R. J., Murphy, E. J., McKinnon, M., et al. 2018, Science with a Next Generation Very Large Array: The ngVLA Reference Design (San Francisco, CA: ASP)
- Spiegelhalter, D. J., Best, N. G., Carlin, B. P., & Van Der Linde, A. 2002, *Journal of the Royal Statistical Society: Series B (Statistical Methodology)*, **64**, 583
- Tollefson, J., de Pater, I., Luszcz-Cook, S. C., et al. 2019, *ApJ*, **157**, 251
- Tollefson, J., de Pater, I., Marcus, P. S., et al. 2018, *Icar*, **311**, 317
- Trafton, L. M. 1967, *ApJ*, **147**, 765
- Wallace, L. 1980, *Icar*, **43**, 231
- Warwick, J. W., Evans, D. R., Peltzer, G. R., et al. 1989, *Sci*, **246**, 1498
- Weidenschilling, S., & Lewis, J. 1973, *Icar*, **20**, 465
- Young, K. C. 1993, *Microphysical Processes in Clouds* (New York: Oxford Uni. Press)